Trees, Forests and People 23 (2026) 101146

Contents lists available at ScienceDirect

Trees, Forests and People

journal homepage: www.sciencedirect.com/journal/trees-forests-and-people

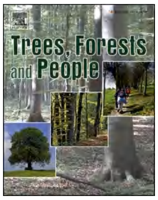

Mask R-CNN-based detection and segmentation of Mangrove ecosystems in Lantau Island, Hong Kong

Renjie Wu [a], Zhijun Dai [a,b,1,*], Xuefei Mei [a], Chuqi Long [c], Diankai Wang [a], Jie Wang [d], Jinping Cheng [c,1,*]

[a] State Key Laboratory of Estuarine and Coastal Research, East China Normal University, Shanghai 200241, China
[b] Laboratory for Marine Geology, Qingdao Marine Science and Technology Center, Qingdao, 266061, China
[c] Department of Science and Environmental Studies, The Education University of Hong Kong, New Territories, Hong Kong, China
[d] State Key Laboratory of Climate Resilience for Coastal Cities, The Hong Kong Polytechnic University, Kowloon, Hong Kong, China

ARTICLE INFO

Keywords:
Mangrove forest
Hydrodynamic actions
Deep learning
Mask R-CNN
Lantau Island

ABSTRACT

Mangroves play a crucial role in coastal protection and biodiversity but face escalating threats from anthropogenic pressures and climate-driven disturbances. Long-term monitoring remains challenging due to mangrove fragmentation and limited high-resolution historical data. This study presents a deep learning–based approach for mangrove identification, leveraging cloud-free Sentinel-2 MSI imagery (10 m resolution) and Mask R-CNN to map and analyze mangrove dynamics on Lantau Island, Hong Kong, from 2016 to 2024. The model integrates surface reflectance bands, spectral indices (EVI, LSWI, MVI), and elevation data, achieving high accuracy (mean absolute percentage error: 6.91%; root mean square error: 0.04×10^4 ha). Multi-source validation demonstrated its strong generalization capacity across global mangrove ecosystems. Spatiotemporal analysis revealed divergent trends in two key mangrove stands. In Shui Hau, mangrove area declined continuously from 0.77 ha in 2016 to 0.39 ha in 2024, accompanied by shoreline erosion at a rate of 3.07 m/yr. This loss was associated with reduced suspended sediment concentration and persistent high wave energy. In contrast, Tung Chung's mangrove area expanded from 3.28 ha to 3.59 ha, with shoreline accretion at 0.85 m/yr, supported by moderate wave dynamics and higher sediment availability. These findings underscore the value of 10 m resolution Sentinel-2 MSI imagery for historical mangrove mapping, providing critical insights for targeted conservation and management strategies.

1. Introduction

Mangroves constitute a distinctive assemblage of salt-tolerant vegetation primarily occupying the intertidal zones of tropical and subtropical coastlines, forming a critical transition interface between terrestrial and marine ecosystems (Donato et al., 2011; Giri et al., 2011). Globally, mangrove forests span approximately 147,000 km^2 of coastal areas (Leal and Spalding, 2022), accounting for less than 1 % of the world's tropical forest cover (Giri et al., 2011; Jennerjahn and Ittekkot, 2002). Despite their relatively limited spatial extent, mangroves play an indispensable role as significant global carbon sinks, contributing substantially to carbon sequestration and thus climate change mitigation (Duarte et al., 2013; Richards et al., 2020). Nevertheless, these vital ecosystems are increasingly threatened by rising sea levels and intensifying anthropogenic pressures (Blankespoor et al., 2017; Goldberg et al., 2020; Monika and Yadav, 2022; Ward et al., 2016). During the latter half of the 20th century, mangrove areas declined at an alarming rate of 1–2 % annually, largely driven by rapid urbanization, industrial development, and the escalating impacts of sea-level rise (Friess et al., 2019; Woodroffe et al., 2016). Therefore, precise mapping and monitoring of mangrove distribution are essential for effective conservation, ecological restoration, and coastal risk assessment.

Some studies have focused on mangrove changes in river deltas and estuaries, whereas mangrove dynamics in marine embayment have received comparatively less attention. In Asia, in certain areas of Indonesia's Subang Regency, mangrove area declined by 83 % between 2017 and 2022 due to aquaculture expansion, with the remaining 17 % of losses attributed to other human activities and natural hazards

---

* Corresponding authors.
E-mail addresses: zjdai@sklec.ecnu.edu.cn (Z. Dai), jincheng@eduhk.hk (J. Cheng).
[1] The corresponding authors contribute equally to this work.

https://doi.org/10.1016/j.tfp.2026.101146

(Dzulfigar et al., 2024). In the Maldives, widespread mangrove dieback occurred in 2020 due to salinity stress from high sea levels and an extreme positive Indian Ocean Dipole event (Carruthers et al., 2024). In contrast, the Beilun Estuary exhibited an overall 11.2 % increase in mangrove area from 1986 to 2022, with localized losses on the landward side offset by seaward expansion behind barrier islands (Long et al., 2025). In Africa, the Niger Delta lost 2536 km^2 of mangroves over the same period, with oil spills accounting for 54.27 % of the losses and urban expansion accelerating landward retreat at 13.58 m/yr (Wang et al., 2025). Ghana's mangrove area declined by 15.4 % between 2015 and 2024, mainly due to urban expansion, indiscriminate waste disposal, wildfires, and uncontrolled sand and salt mining (Ofori et al., 2025). In North America, Florida's mangroves declined by 547.3 km^2 from 1986 to 2022, mainly due to major storms, while sea-level rise played a minimal role (Liang et al., 2025). In South America, coastal Guyana recorded a net mangrove gain of 0.09 km^2 from 2013 to 2022, primarily driven by restoration initiatives (Hamer et al., 2024). Oceania's Fly River Delta lost 33.83 % of its mangroves from 1988 to 2023, with 54.71 % of coastal losses attributed to wave action and human activity, despite local seaward gains (Wu et al., 2025). These divergent patterns underscore the complexity of mangrove dynamics, shaped by interactions among sediment supply, wave energy, land use, and extreme weather events (Hagger et al., 2022).

The understanding of the spatial-temporal characteristics of mangrove ecosystems plays a critical role in determining appropriate protection measures or restoration plans (Ellison et al., 2020; Jia et al., 2014; Zhang et al., 2023). However, accurately mapping the spatial distribution of mangroves and continuously monitoring their temporal dynamics are fundamental prerequisites for designing effective conservation and restoration strategies (Ellison et al., 2020; Jia et al., 2014; Zhang et al., 2023). Previous studies have employed a range of approaches—including field surveys and remote sensing—to quantify mangrove extent and assess ecological changes over time (Robertson et al., 1991). Yet, field-based measurements are often constrained by difficult terrain, limited accessibility, and the inability to capture regional-scale variations, particularly in complex intertidal environments (Giri, 2016). Deep learning methods help overcome key challenges in mangrove interpretation by improving the discrimination of spectrally similar vegetation, enhancing boundary delineation in fragmented coastal landscapes, and enabling more reliable detection of subtle ecological changes that traditional remote sensing approaches may overlook (Anees et al., 2025; Kirui et al., 2013; Mehmood et al., 2025). Recently, there has been rapid development in using deep-learning-based algorithms for mangrove mapping based on coastal and wetland images. Xu et al. (2023) combined time series Landsat data and the MSNet semantic segmentation algorithm to obtain spatiotemporal change information about mangrove coverages. Zhang et al. (2025) used high-resolution optical image data along with the DeepLab

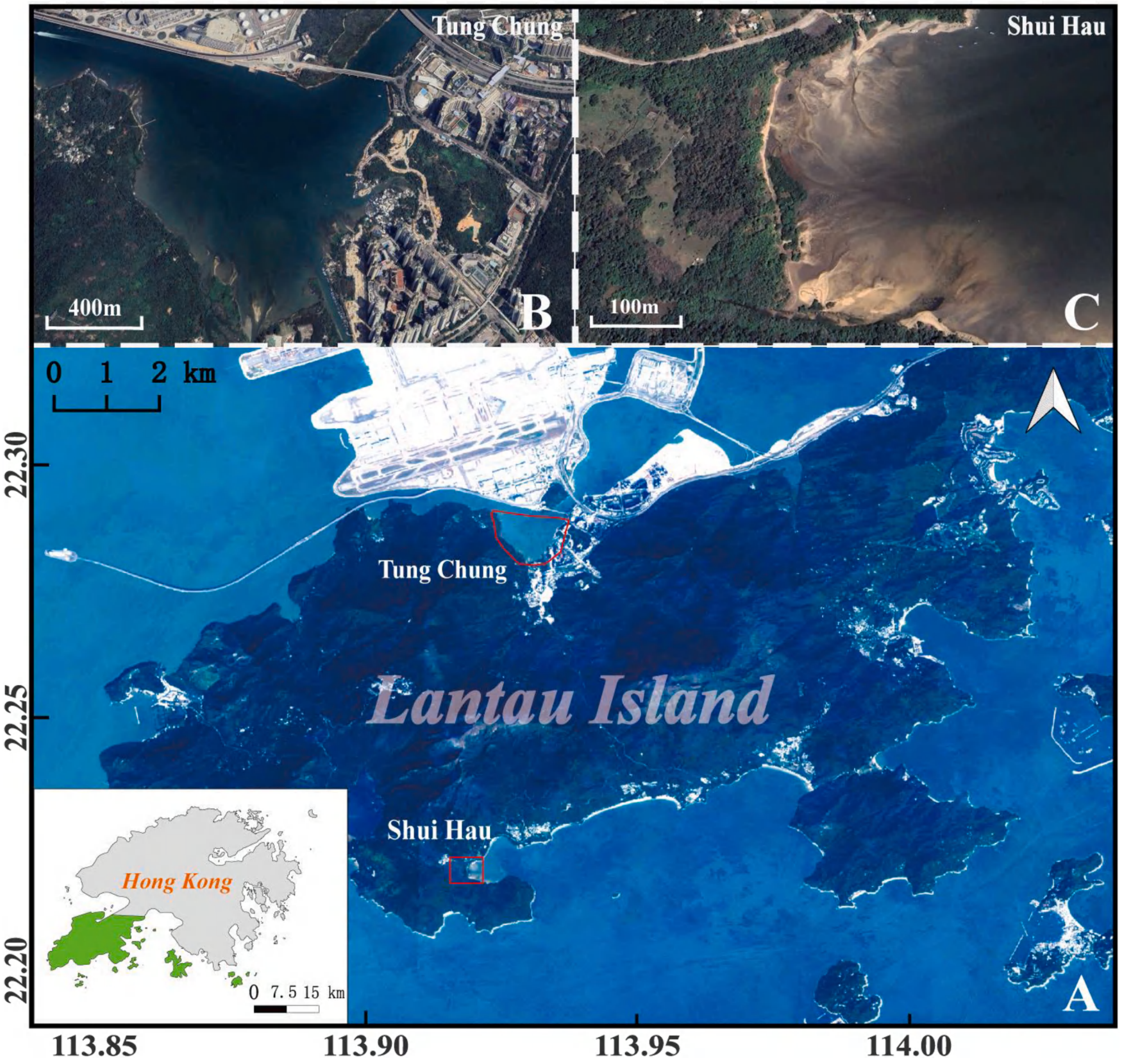

Fig. 1. A: Location of the Lantau Island. B: Tung Chung. C: Shui Hau.

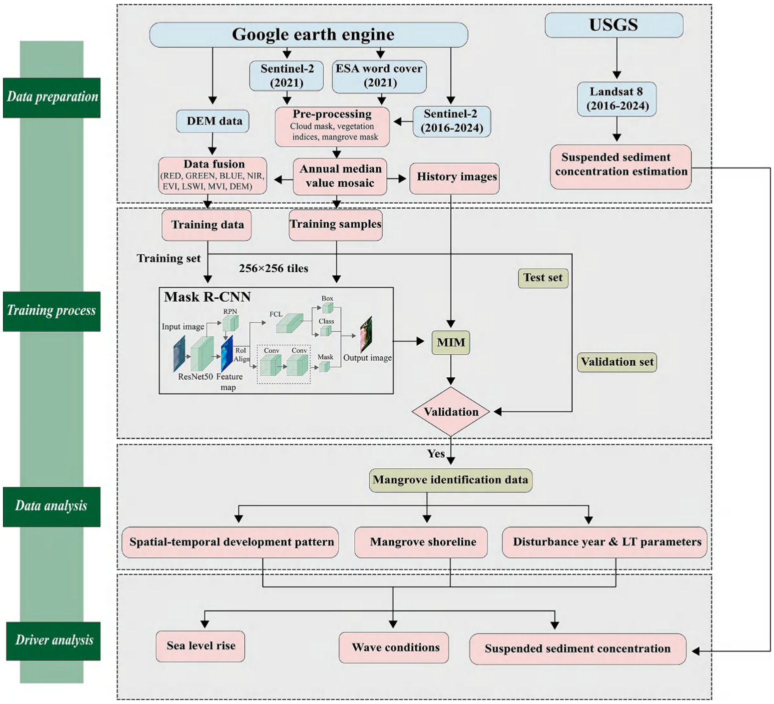

Fig. 2. Workflow employed in the study.

V3+ instance segmentation method to detect the mangrove area accurately. One of the advantages of the deep learning approach is that it can automatically extract hierarchical features from raw inputs without any human intervention, which reduces the requirement of hand-crafted features and enables fast and efficient model training (Zhao et al., 2024). But semantic segmentation networks usually suffer low boundary accuracy than instance segmentation ones (Yin et al., 2022). Therefore, we choose the instance segmentation framework as our network structure to achieve accurate detection results of mangroves in this paper.

Mask R-CNN is simple but effective end-to-end architecture that can simultaneously detect instances in images and generate high quality mask prediction maps for all detected instances (He et al., 2017), which makes it ideal for many remote sensing problems such as those dealing with complex land covers. Recently, Mask R-CNN has become popular for instance level object detection and segmentation on high resolution satellite images because it can joint optimize object localization and semantic boundaries (Han et al., 2022; Liu et al., 2022). Also, it shows promising results when applied on VHR dataset composed by VNIR bands with an accuracy higher than 91.4 % and an f-score greater than 0.89 in the mangrove canopy segmentation task (Lassalle and De Souza Filho, 2022). Moreover, the mangrove communities on Lantau Island are relatively sparse and often occur in small (Zhang et al., 2025). Mask R-CNN treats each mangrove patch as an individual instance, enabling the model to preserve fine boundary details, discriminate between closely adjacent patches, and prevent the merging of spectrally similar yet spatially distinct vegetation groups (Carvalho et al., 2020; Yin et al., 2022). All these reasons motivate us to choose Mask R-CNN for our mangrove delineation problem.

The reliable spatiotemporal description of mangroves is an important prerequisite for formulating appropriate management and conservation measures against environmental stresses (Wu et al., 2025). The launch of Sentinel-2 in 2015 provided us with free-of-charge, high spatial resolution(10 m), multi-spectral imaging every five days at global scale, which makes it suitable for investigating the dynamic change of small areas such as mangrove ecosystems (Phiri et al., 2020). Therefore, we use time series of Sentinel-2 Multi-Spectral Instrument (MSI) data combined with a deep learning-based instance segmentation network Mask Region Convolutional Neural Network (MaskR-CNN) to study the dynamics of mangroves on Lantau Island, Hong Kong from 2016 to 2024.

On Lantau Island, the sediment supply is controlled mainly by local terrestrial input and nearshore hydrodynamics (Xiong et al., 2018). Sediment fluxes control both sediment transport and deposition processes, which affect mangroves' distributions (Fanous et al., 2023; Krauss et al., 2014). In areas of relatively weak energy along coastlines, fine-grained sediments may be deposited on the intertidal zone or estuaries resulting from the accumulation of sediment during flooding cycles, causing elevating of substrate surface level for the expansion of mangroves towards seawards (Walsh and Ridd, 2008; Wolanski et al., 2006). However, in areas of higher energy conditions, waves and turbulence cause erosion that inhibits seedlings establishment and prevents the colonization of mangroves (Mbense et al., 2016; Raw et al., 2019). Apart from hydrodynamic factors, sea-level rise has emerged as a key driver of landward retreat, particularly where vertical accretion fails to keep pace with rising water levels (Fanous et al., 2023; Gilman et al., 2007). Moreover, extreme weather events such as typhoons have caused severe damage to mangrove canopies (Kauffman and Cole, 2010; Paling et al., 2008).

Thereafter, the analysis focuses on two representative mangrove stands—Shui Hau and Tung Chung—and aims to (1) assess the performance of the Mask R-CNN model in mangrove mapping through quantitative accuracy metrics; (2) quantify spatiotemporal variations in mangrove extent in Shui Hau and Tung Chung from 2016 to 2024; (3) identify the primary environmental factors driving mangrove expansion and retreat in each region; and (4) compare the performance of instance segmentation (Mask R-CNN) with semantic segmentation models in delineating mangrove boundaries. Through this work, we seek to enhance understanding of small-scale mangrove dynamics and support the development of targeted conservation strategies, while also providing insights into the broader applicability of deep learning models for biophysical mapping in dynamic coastal systems.

Table 1
Summary of datasets used in this study.

Dataset	Source	Time period
Sentinel-2 MSI	GEE	2016–2024
ESA WorldCover v2.0	GEE	2021
Copernicus DEM GLO-30	GEE	2010–2015
Landsat 8 OLI	USGS	2016–2024
ECMWF wave data	ECMWF	2016–2024
Sea level data (Shek Pik)	Hong Kong Observatory	1998–2024
Google earth Imagery	Google earth	2021
Global mangrove watch	Zenodo	1996–2020

2. Materials and methods

2.1. Study area

Situated in southeastern China at the mouth of the Pearl River Delta, Hong Kong is a key component of the Greater Bay Area and hosts approximately 60 mangrove stands across six districts, including Lantau Island (Zhang et al., 2025). The study area focuses on Shui Hau and Tung Chung, two mangrove stands located on Lantau Island, the largest island in Hong Kong (Fig. 1). Lantau Island's coastal topography, characterized by a mix of mountainous terrain and flat intertidal zones, creates unique conditions for mangrove ecosystems. Both Shui Hau and Tung Chung are situated along Hong Kong’s western coastline and are subject to varying degrees of influence from the Pearl River Estuary. Shui Hau lies within a relatively enclosed embayment on southern Lantau Island, where hydrodynamic exchange is weak (Fig. 1), whereas Tung Chung is located adjacent to the airport and experiences more complex tidal and hydrodynamic conditions (Vorsatz et al., 2023; Wang et al., 2023). Despite hosting multiple mangrove species—including Kandelia candel, Aegiceras corniculatum, Avicennia marina, Bruguiera gymnorrhiza, Excoecaria agallocha, and Acanthus ilicifolius—their mangrove patches remain small, fragmented, and characterized by simple community structures. Such ecological attributes have long been overlooked in traditional mangrove studies, which typically focus on larger and better-conserved stands (Tam et al., 1997).

2.2. Materials

This study utilized multiple remote sensing and auxiliary datasets, each serving different analytical purposes throughout the model training, validation, and mangrove dynamics assessment workflow (Fig. 2). A summary of all datasets is presented in Table 1. First, cloud-free Sentinel-2 MSI imagery (2021) was downloaded from Google Earth Engine (GEE) and used as the primary input for training the mangrove identification model (code:https://github.com/CousinRock/Download-S2-for-mangrovedetection.git). The mangrove label data were derived from the 2021 ESA WorldCover v2.0 product (ESA_WorldCover_v200). To account for terrain effects on mangrove distribution, the Copernicus DEM GLO-30 dataset was used to extract elevation information (Copernicus DEM GLO-30). To ensure label reliability, all training samples were visually inspected using 2021 Sentinel-2 imagery and high-resolution Google Earth imagery, and areas showing obvious inconsistencies were manually removed. In addition, the Global Mangrove Watch (GMW) dataset (1996–2020) was consulted as a long-term spatial reference to verify the stability and plausibility of mangrove distribution patterns (Bunting et al., 2022). For suspended sediment concentration (SSC) estimation, all available cloud-free Level-1 Landsat 8 OLI images over Lantau Island (2016–2024) were acquired from the USGS Earth Explorer platform (https://earthexplorer.usgs.gov/). Hydrodynamic and tidal conditions were characterized using ECMWF wave products (mean wave direction and significant wave height)(https://cds.climate.copernicus.eu) and sea level records from the Hong Kong Observatory (https://www.hko.gov.hk). In addition, three spectral indices—Enhanced Vegetation Index (EVI), Land Surface Water Index (LSWI), and Mangrove Vegetation Index (MVI)—were calculated to enhance the spectral separability between mangrove and non-mangrove features. The formulas for calculating the three spectral indices are as follows:

$$\mathrm{EVI} = 2.5\frac{\mathrm{NIR} - \mathrm{RED}}{\mathrm{NIR} + 6\mathrm{RED} - 7.5\mathrm{BLUE} + 1} \tag{1}$$

$$\mathrm{LSWI} = \frac{\mathrm{NIR} - \mathrm{SWIR1}}{\mathrm{NIR} + \mathrm{SWIR1}} \tag{2}$$

$$\mathrm{MVI} = \frac{\mathrm{NIR} - \mathrm{GREEN}}{\mathrm{SWIR1} - \mathrm{GREEN}} \tag{3}$$

where RED, GREEN, BLUE, NIR, and SWIR1 respectively represent the pixel values of the red, green, blue, near-infrared, and short-wave infrared bands.

2.3. Methods

2.3.1. Mangrove identification model training

2.3.1.1. Input data preparation. The mangrove identification model (MIM) was established by adapting the Mask Region-based Convolutional Neural Network (Mask R-CNN), an instance segmentation framework that extends Faster R-CNN by integrating a parallel mask prediction branch for pixel-level segmentation alongside object detection (Wang and He, 2022). Compared with semantic segmentation networks such as FCN, Mask R-CNN achieves higher boundary precision through the RoIAlign operation (Fig. 2), which eliminates the spatial quantization errors of traditional RoIPool and enables precise pixel-to-pixel alignment between input features and predicted masks. This operation significantly enhances localization accuracy, improving mask performance by 10–50 % under stricter metrics (He et al., 2017), and thus provides a clear advantage in detecting fine and irregular boundaries. In the context of mangrove ecosystems, where vegetation often occurs in fragmented, patchy structures interspersed with water and mudflats, such fine boundary discrimination becomes crucial (Wu et al., 2025; Xiong et al., 2024). Instance segmentation models like Mask R-CNN have demonstrated strong performance in these heterogeneous environments—Lassalle & De Souza Filho (2022) successfully applied Mask R-CNN to delineate mangrove canopy gaps with high accuracy (F1 $\geq$ 0.89)—indicating its robustness in distinguishing discrete mangrove patches and their boundaries within complex coastal mosaics. This architecture is well-suited for remote sensing applications, as it supports multi-channel inputs and large-scale geospatial analysis (Carvalho et al., 2020). To streamline geospatial data processing, the study employed GeoAI, an open-source Python package designed to bridge AI and geospatial analysis through advanced machine learning tools (Wu, 2025). Input data consisted of Sentinel-2 MSI surface reflectance bands (blue, green, red, and near-infrared), supplemented by three spectral indices calculated using geemap (Wu, 2020): the Enhanced Vegetation Index (EVI) to isolate vegetation from soil and water (Huete et al., 2002), and the Land Surface Water Index (LSWI) to highlight water-rich features like mangroves (Chandrasekar et al., 2010), and the Mangrove Vegetation Index (MVI) to distinguish mangroves from other land covers (Baloloy et al., 2020), along with elevation data from the Copernicus DEM GLO-30. EVI can effectively separate vegetation from soil and water, providing advantages for vegetation detection and feature extraction. LSWI is sensitive to the liquid water content in vegetation and soil, highlighting water-rich areas such as mangroves. MVI is specifically designed to distinguish mangroves from non-mangrove vegetation and other non-vegetated surfaces, enhancing classification accuracy in complex coastal landscapes (Xiong et al., 2024). Although the ESA WorldCover v2.0 product provides globally consistent mangrove masks, all training samples and test regions were visually inspected using Sentinel-2 MSI imagery from 2021 and high-resolution

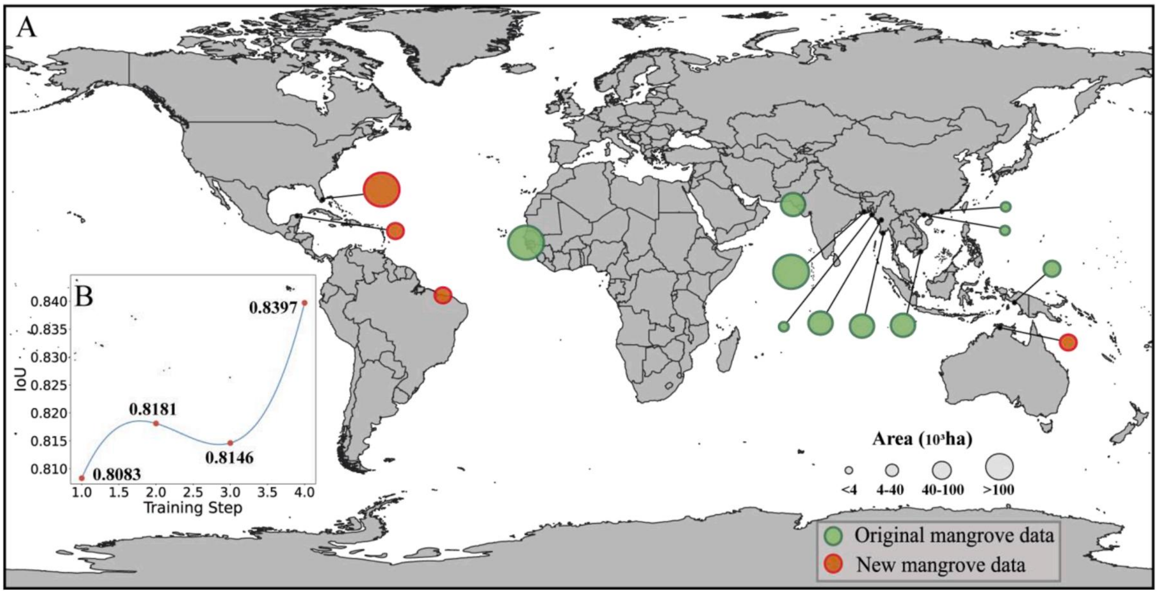

Fig. 3. Model training and dataset preparation. A: Training dataset samples distribution. B: Optimization of the mangrove identification model.

Google Earth imagery to ensure temporal consistency with the label data. The Global Mangrove Watch dataset (1996–2020) was additionally consulted as a stable long-term spatial reference to contextualize mangrove distribution patterns. Areas exhibiting evident misclassification in the 2021 imagery were removed prior to training. Furthermore, the performance of the MIM was evaluated using independent high-resolution external datasets rather than relying solely on the WorldCover labels, ensuring that the validation metrics are not affected by potential label uncertainties.

2.3.1.2. Training parameters and fine-tuning strategy. For model training, we selected cloud-free images from ten global regions and merged them before tiling into 256 × 256 pixel tiles, ultimately generating 14,342 image-label pairs (Fig. 3A). The dataset was split with 80 % for training and 20 % for validation. The model was trained using a ResNet-50 backbone integrated with a Feature Pyramid Network (FPN). Training was performed with a batch size of 4 using stochastic gradient descent (SGD) optimization, and an initial learning rate schedule that decayed by a factor of 0.8 every five epochs. The initial mangrove identification model was trained using Mask R-CNN for 45 epochs with a learning rate of 0.0001. Subsequent fine-tuning involved three phases. During all fine-tuning stages, the batch size remained 4 and the same learning rate decay schedule was maintained. The first phase increased the learning rate to 0.001 and training for an additional 50 epochs on the original dataset; second, keeping the epoch count and learning rate constant while expanding the dataset with cloud-free images from additional regions (adding 3736 images with corresponding labels); and finally, maintaining the learning rate at 0.001 while increasing the number of training epochs to 60 for further optimization. The model achieving the highest IoU across all training and fine-tuning phases was selected as the final mangrove identification model (Fig. 3B).

2.3.2. Mangrove dynamic analysis

2.3.2.1. Shoreline change calculation. In order to quantitatively analyze the changes in shoreline position during our research area within the study period, we applied the Digital Shoreline Analysis System (DSAS) (developed by USGS) which is one of the tools that are integrated into ArcGIS. It has been widely adopted worldwide because it offers many statistical methods based on multi-time shoreline data. In this paper, we use the historical mangrove shoreline information extracted via remote sensing as input to DSAS (Wu et al., 2025). Then, among these statistics, linear regression rate (LRR)was chosen to be the main metric to calculate the long-term shoreline change trends due to its wide application and high accuracy. The LRR refers to the slope coefficient calculated with Least Square Method fitting all shoreline points along each transect into a straight line, so it can represent the overall trend of shoreline evolution during the whole timespan (Himmelstoss et al., 2021). If the LRR <0 then there will exist an erosion tendency at the shoreline, meaning that the mangrove shorelines tend to move towards inland. On the contrary if the LRR>0 means that the shoreline is moving towards sea direction due to deposition process. To determine the possible impacts of mangrove forests in comparison with sea level rise, the average vertical sediment accumulation (AVSA) rate was calculated using the following formula (Xiong et al., 2024):

$$\mathrm{AVSA} = \mathrm{V}\tan\theta \tag{4}$$

where V is the average accretion rate of shorelines, and θ is the average slope in the Shui Hau and Tung Chung obtained from DEM.

2.3.2.2. Vegetation health assessment. The Transformed Chlorophyll Absorption in Reflectance Index (TCARI) can reflect the change of chlorophyll contents and photosynthesis activities of plants effectively, thus it serves well as a proxy variable for vegetation health status (Sharifi, 2020). In this study, the LandTrendr (LT) approach based on Sentinel-2 data has been used to extract disturbance pattern at different time scales from mangroves lost or gained area by analyzing spatio-temporal trajectory of spectral indices to determine whether there were any abrupt or slow changes (Chen et al., 2025). LT, as a temporal segmentation algorithm designed for time-series remote sensing data, models pixel-level spectral trajectories as a series of connected linear segments. This enables the extraction of both sudden disturbances and long-term subtle changes in vegetation dynamics (Kennedy et al., 2010). When combined with TCARI, LT first identifies zones of mangrove disturbance or recovery through spectral trajectory segmentation. TCARI's sensitivity to chlorophyll content is then used to infer vegetation health within these LT-identified segments: negative TCARI trends reflect declines in chlorophyll and degraded vegetation health, whereas positive trends indicate recovery or improved physiological condition. By combining the trend of TCARI with LT results, we could assess the dynamic variation of vegetation vigor and health condition over mangroves. The formula for calculation of TCARI is shown below:

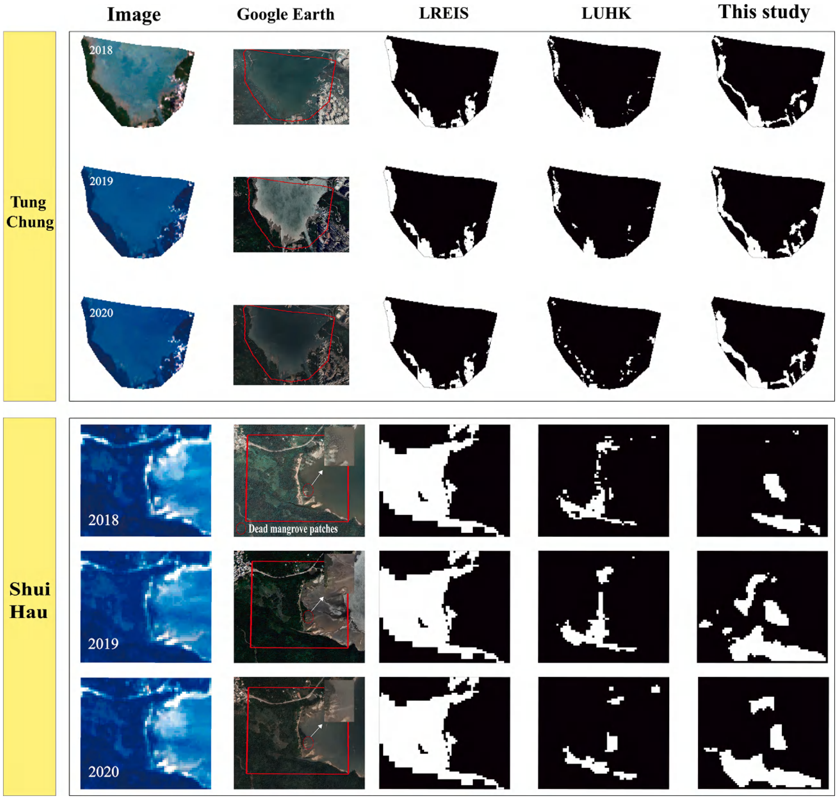

Fig. 4. Comparison of mangrove distribution maps from various sources.

$$\mathrm{TCARI} = 3[((\mathrm{EDGE} - \mathrm{RED}) - 0.2)(\mathrm{EDGE} - \mathrm{GREEN})(\mathrm{EDGE}/\mathrm{RED})] \tag{5}$$

where RED, GREEN, and EDGE respectively represent the pixel values of the red, green, red edge bands.

2.3.3. Remote sensing SSC estimation model

To estimate suspended sediment concentration (SSC) in the Shui Hau and Tung Chung, we adopted the Semi-Empirical Radiative Transfer (SERT) model, which has been validated for turbid estuarine waters (Luo et al., 2022). Previous publications (Pan et al., 2018; Tang et al., 2019) have successfully demonstrated the potential of using the SERT model in turbid waters. Due to the small quantity of high-quality cloudless Landsat images available each year, and this study analyzes and discusses multi-year SSC changes, and do not focus on short time scale processes. Therefore, we averaged the SSC in the Shui Hau and Tung Chung from the Landsat images (time interval of every four years) to obtain the interannual time series SSC distribution. The SSC was estimated using Eq. (6) as follows:

$$\mathrm{SSC} = \frac{2 \times \alpha \times R_{rs}}{\beta \times (\alpha - R_{rs})^2} \tag{6}$$

where SSC is the suspended sediment concentration in g/L, R_{rs} is the atmospherically corrected remote sensing reflectance in sr^{-1}, and α, β are empirical coefficients specific to Landsat-8 OLI Band 4 (655 nm): $\alpha = 0.0763$, $\beta = 11.5306$ (Luo et al., 2022).

2.3.4. Precision assessment

In remote sensing data analysis, ensuring the accuracy and reliability of the results is of paramount importance (Wu et al., 2025). To validate the annual mangrove mapping results derived using the MIM, we implemented a comprehensive and standardized accuracy assessment procedure. Specifically, Sentinel-2 MSI imagery from 15 representative regions was analyzed using the MIM. The resulting mangrove segmentation were compared with the mangrove area data from the ESA dataset to assess spatial consistency and accuracy. Furthermore, to enhance the validation process, visual verification was performed using supplementary datasets comprising Google Earth imagery from 2018 to 2020, the LREIS Global Mangrove dataset (2018–2020) (Xiao et al., 2021), and the Land Utilization in Hong Kong (LUHK) mangrove dataset covering the same period. This multi-source validation approach enhances the credibility and robustness of the results. To comprehensively evaluate the performance of the MIM, both pixel-level and area-level metrics were employed. During model training and selection, the IoU served as the primary segmentation metric to ensure accurate mask learning (Fig. 3B). For the final validation stage, area-based accuracy measures were further introduced to assess the agreement between predicted and reference mangrove extents at the regional scale. Specifically, the mean absolute percentage error (MAPE) and root mean square error (RMSE) were calculated between the predicted and reference mangrove extents. Smaller MAPE indicates better modeling results, and smaller RMSE denotes higher prediction accuracies. These accuracy criteria are calculated as (Zheng et al., 2016):

$$\mathrm{MAPE} = \frac{1}{n}\sum_{i=1}^{n}\left|\frac{y_i - y_i'}{y_i}\right| * 100\% \tag{7}$$

$$RMSE = \sqrt{\frac{1}{n}\sum_{i=1}^{n}(y_i - y_i')^2} \tag{8}$$

where, n is the number of samples, and y_i and y_i' refer to the measured and predicted values for the i th sample.

3. Results

3.1. Validation of MIM

The validation of the MIM was conducted using a multi-source

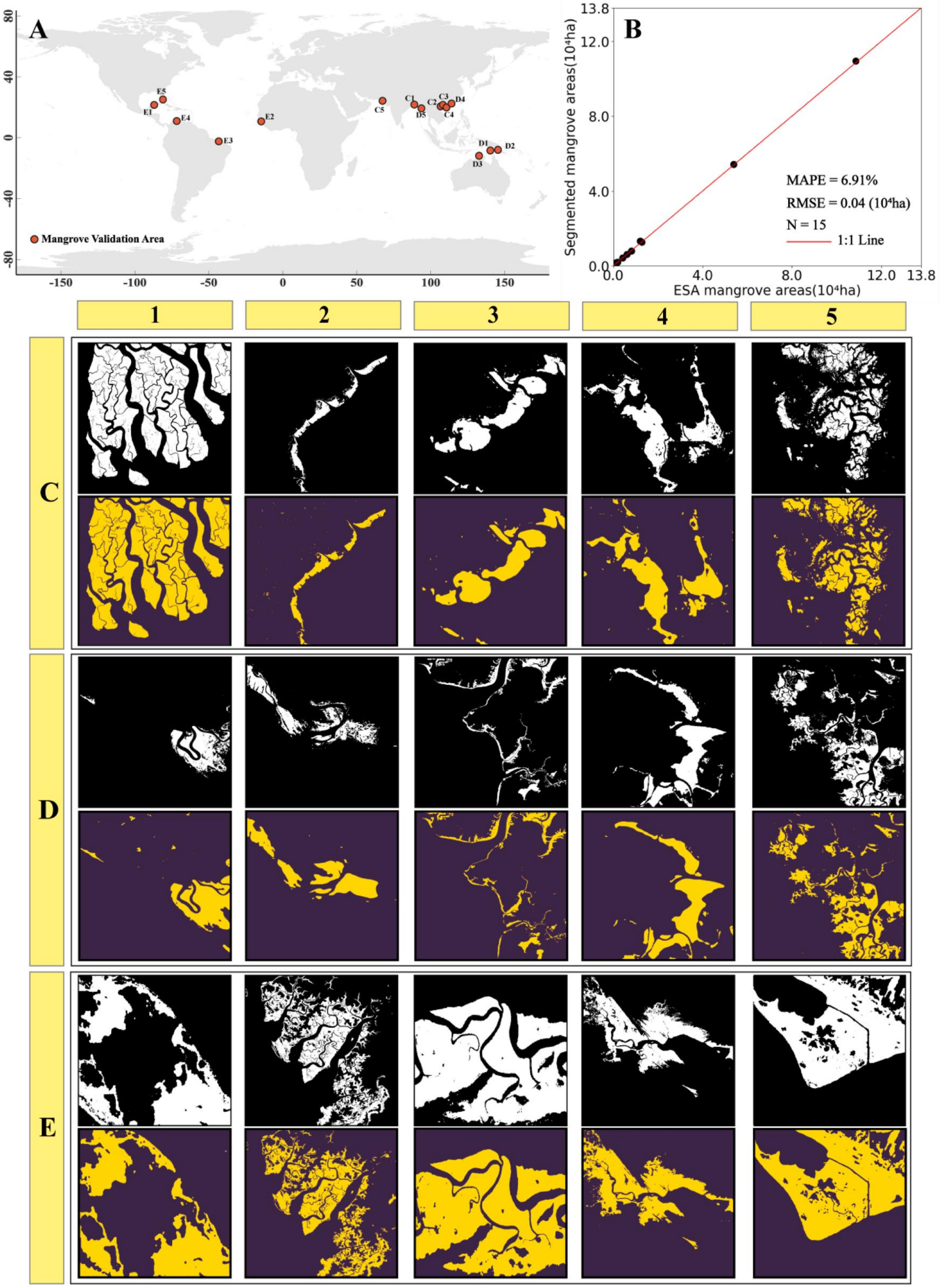

Fig. 5. Validation of MIM across global mangrove regions. A: Locations of 15 validation regions. B: Comparison between predicted and reference mangrove areas. C–E: Representative segmentation examples in different geomorphic settings, illustrating that the predicted mangrove distributions closely match the reference spatial patterns (white represents reference mangrove extent; yellow indicates predicted results).

approach, incorporating Sentinel-2 MSI imagery from 15 diverse regions (Fig. 5A) and high-resolution validation datasets for the Shui Hau and Tung Chung from 2018 to 2020, including Google Earth imagery, the LREIS Global Mangrove dataset (2018–2020), and LUHK mangrove raster grid (Fig. 4). However, visual inspection of high-resolution Google Earth imagery in the Shui Hau area reveals fragmented and dying mangrove patches near the seaward edge (Fig. 4) that are not identified by the LREIS and LUHK datasets. These 15 validation regions are strategically distributed across global mangrove biomes, encompassing North America, West Africa, South Asia, and Southeast Asia and

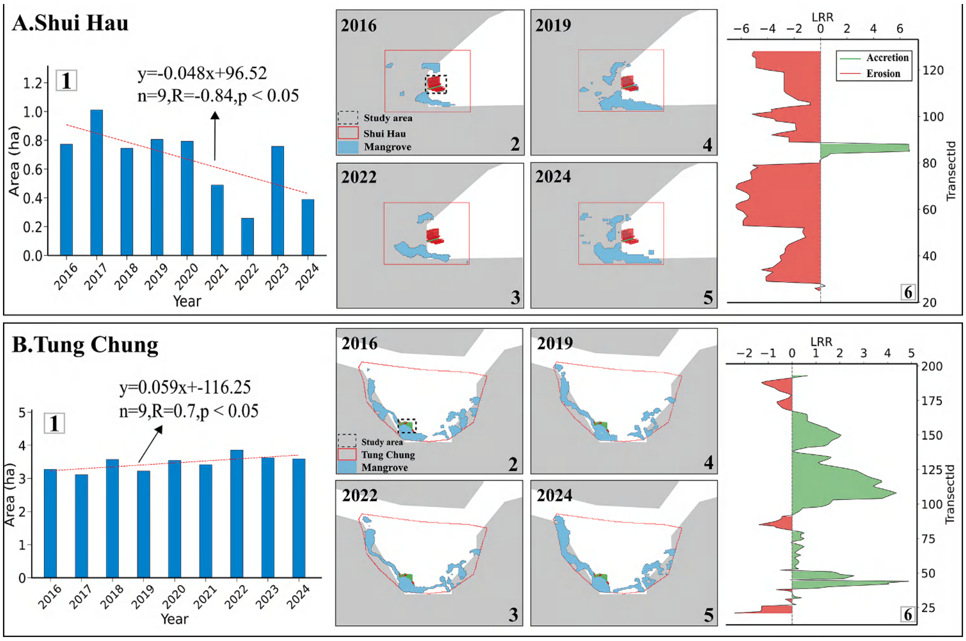

Fig. 6. Spatiotemporal dynamics of mangrove area and shoreline change in Shui Hau and Tung Chung (2016–2024). A1–B1: Temporal changes in mangrove area. A2–A6 and B2–B6: Erosion and accretion segments along the mangrove shoreline and spatial distribution of shoreline movement rates.

Oceania, as indicated on the world map (Fig. 5A). They span a diverse range of geomorphological settings, including estuaries, deltas, and bays, ensuring that the model is tested under heterogeneous environmental conditions. Comparative analysis revealed strong agreement between MIM-derived mangrove segmentation and ESA reference datasets (Fig. 5C-E), with both datasets mangrove area closely aligned along the 1:1 line (Fig. 5B), demonstrating the model's robust spatial consistency. In particular, the model accurately captured both compact and fragmented mangrove distributions across varied coastal landscapes. For instance, in deltaic environments (Fig. 5C1, C5, E2), the MIM preserved the intricate boundary structures and narrow tidal creeks, while in narrow estuarine channels (Fig. 5C2, D4), the segmentation results remained continuous and coherent. Quantitative assessment yielded a mean absolute percentage error (MAPE) of 6.91 % and a root mean square error (RMSE) of 0.04×10^4 ha for mangrove area estimation, indicating high prediction accuracy (Fig. 5B).

External datasets were used as complementary references. These datasets provide high-resolution or standardized baselines, which can help contextualize and cross-check the model outputs. While some fragmented or degraded mangrove patches may not be captured by these datasets, they still offer useful guidance for evaluating the general spatial distribution of mangroves. Together, the external datasets and model predictions provide a more comprehensive assessment of mangrove extent. When benchmarked against existing mangrove studies in the Shui Hau and Tung Chung regions, the spatial distribution of mangroves extracted in this research shows high consistency with the coastal ecological unit characterization of Shui Hau Village presented (Ho and Chung, 2025). Meanwhile, the mangrove distribution ranges in both Shui Hau and Tung Chung can be spatially matched with the mangrove sample points derived from ultra-high-resolution imagery (Zhang et al., 2025), providing direct localized validation for the model's applicability and reliability in regional mangrove mapping. This comprehensive validation, integrating global, regional, and very-high-resolution satellite references, conclusively demonstrates the model's effectiveness in mangrove identification, providing a reliable foundation for subsequent spatiotemporal analysis of Shui Hau and Tung Chung mangrove ecosystems. The model's strong performance ensures accurate detection of both subtle and pronounced changes in mangrove distribution patterns over time.

3.2. *Variations in mangrove area and shoreline dynamics*

To accurately characterize the mangrove change trends in Shui Hau and Tung Chung, we first delineated the most stable core regions from the annual mangrove identification results over 2016–2024 as the focal study areas (Fig. 6). Given that the mangrove patches in these sites are spatially small and the regional-scale RMSE of the MIM results is 0.04×10^4 ha (Fig. 5B), the analysis focused on stable mangrove zones to minimize classification uncertainty caused by spatial resolution limitations. To ensure that the detected trends represented genuine ecological change rather than model artifacts, historical Google Earth imagery was visually interpreted, and only the core regions that remained consistently recognizable across years were retained for detailed analysis. From 2016 to 2024, the mangrove ecosystems in Shui Hau and Tung Chung exhibited markedly divergent trajectories in both area and shoreline dynamics (Fig. 6A1–B1). Specifically, the mangrove area in Shui Hau demonstrated a continuous decreasing trend, shrinking from 0.77 ha in 2016 to just 0.39 ha by 2024—an average annual loss of approximately 0.048 ha (Fig. 6A1). In contrast, Tung Chung experienced a gradual increase in mangrove area, expanding from 3.28 ha in 2016 to 3.59 ha in 2024, corresponding to a mean annual increase of 0.059 ha (Fig. 6B1).

However, mangrove shoreline-level assessments revealed more nuanced patterns of mangrove change in both regions. In Shui Hau, shoreline dynamics were dominated by erosion, with eroding segments accounting for 92 % of the total mangrove shoreline count while accretional segments represented only 8 % (Fig. 6A2-A5). Conversely, Tung Chung exhibited a predominantly accretional trend, where expanding shoreline segments constituted 72 % of the total count, significantly outweighing eroding segments at 28 % (Fig. 6B2-B5). The contrasting patterns were further reflected in the spatial dynamics of mangrove shorelines. Along the Shui Hau coast, the mangrove shoreline predominantly retreated between 2016 and 2024, indicative of widespread erosion (Fig. 6A6). The average shoreline retreat rate was −3.07 m/yr, with peak erosion reaching up to 6.41 m/yr. In contrast, Tung Chung's mangrove shoreline exhibited signs of progradation in several sectors, with an average expansion rate of 0.85 m/yr and a maximum seaward advance of 4.87 m/yr (Fig. 6B6). In comparison to the Tung Chung, the Shui Hau is undergoing more severe mangrove degradation

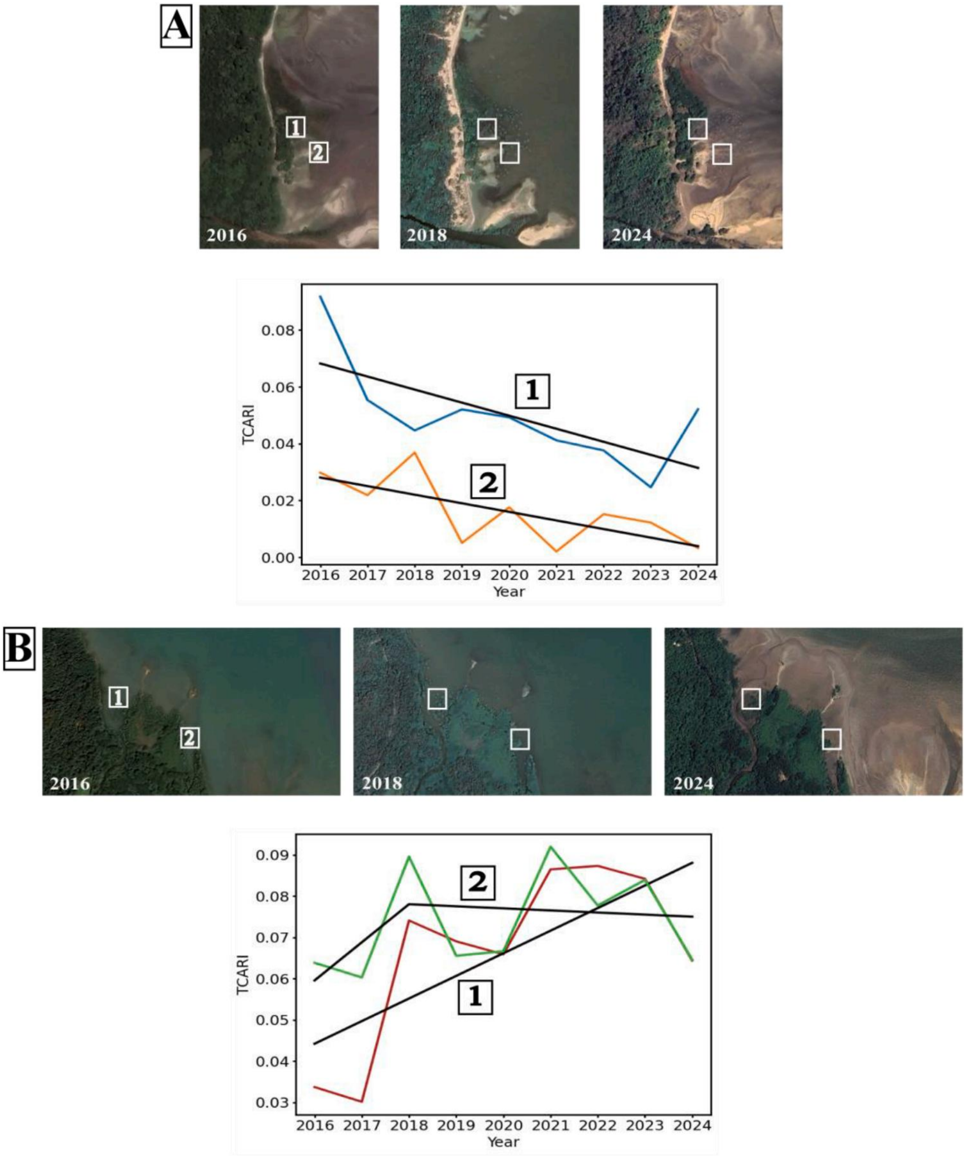

Fig. 7. Mangrove change and vegetation health analysis using LandTrendr and TCARI index. A: Temporal trends of vegetation decline in Shui Hau. B: Vegetation recovery and stabilization patterns in Tung Chung.

and shoreline erosion. Notably, the contrasting trends of mangrove loss in Shui Hau and gain in Tung Chung are not random, but are likely driven by differences in local environmental conditions that govern mangrove growth and survival, including variations in the intensity of hydrodynamic forces acting on the shorelines, the availability of sediment for substrate accretion, and potential anthropogenic disturbances that may affect habitat suitability.

3.3. *Example segmentation results*

As expected, the LT algorithm effectively captured abrupt disturbance events, including both mangrove loss and expansion, as well as changes in vegetation health status as indicated by the TCARI index (Fig. 7). In Shui Hau, within areas that experienced mangrove loss, the LT outputs revealed a consistent decline in TCARI values over time, reflecting a gradual deterioration in vegetation health. Specifically, both subregions (labeled 1 and 2) exhibited decreasing TCARI trends from 2016 to 2024 (Fig. 7A), consistent with the observed retreat of mangrove area. In contrast, mangrove gain regions in Tung Chung showed two distinct temporal patterns (Fig. 7B). In subregion 1, mangroves expanded seaward from 2016 to 2024 (Fig. 6B7), accompanied by a steady increase in TCARI values, suggesting progressive improvement in vegetation vigor. In subregion 2, mangroves exhibited expansion between 2016 and 2018, followed by relatively stable coverage from 2018 to 2024. Correspondingly, TCARI values increased during the early period but plateaued thereafter, indicating a stabilization in vegetation health (Fig. 7B).

4. Discussion

4.1. *Comparing different models*

To the best of our knowledge, this study represents the first application of deep learning–based instance segmentation using Sentinel-2 MSI imagery for mangrove mapping on Lantau Island. To benchmark the performance of the Mask R-CNN model, additional models—including Unet, FPN, DeepLabV3, and DeepLabV3+—were trained using the same dataset. Importantly, the semantic segmentation models were deliberately trained until their validation IoU exceeded that of Mask R-CNN. IoU, although an important metric, has inherent

Table 2
Accuracy comparison of different mangrove segmentation models.

	Unet	FPN	DeepLabV3	DeepLabV3+	MaskR-CNN
OA	0.9031	0.9192	0.9281	0.9202	**0.9434**
Precision	0.6658	0.7127	0.7399	0.7162	**0.8015**
Recall	0.945	0.936	0.9358	0.9337	**0.9184**
F1-Score +	0.7812	0.8092	0.8264	0.8106	**0.8559**
IoU	0.6409	0.6796	0.7041	0.6816	**0.7482**
Non-Mangrove precision	0.9864	0.9846	0.9847	0.9841	**0.9811**
Non-Mangrove recall	0.8938	0.9155	0.9263	0.9171	**0.949**
Non-Mangrove F1-Score	0.9378	0.9488	0.9546	0.9494	**0.9648**
Non-Mangrove IoU	0.8829	0.9025	0.9132	0.9037	**0.932**

limitations in evaluating segmentation performance—particularly in its inability to capture false positives, boundary accuracy, and fine-scale structural preservation (Zhang et al., 2022). Therefore, we include additional assessment metrics to more comprehensively evaluate model effectiveness. When evaluated across multiple metrics, Mask R-CNN demonstrated competitive and robust performance across multiple metrics, achieving an overall accuracy (OA) of 94.34 %, a precision of 80.15 %, and an F1-Score of 85.59 %. Notably, the precision of Mask R-CNN exceeded that of Unet by 13.57 %, FPN by 8.88 %, DeepLabV3 by 6.16 %, and DeepLabV3+ by 8.53 %. These results suggest that while other models may offer marginally higher IoU, Mask R-CNN excels in correctly identifying mangrove pixels with fewer false positives. For non-mangrove pixels, Mask R-CNN also demonstrated superior performance, achieving a precision of 98.11 %, a recall of 94.9 %, an F1-Score of 96.48 %, and an IoU of 93.2 %. Compared to DeepLabV3, DeepLabV3+, FPN, and Unet, Mask R-CNN's non-mangrove F1-Score was higher by 1.02 %, 1.54 %, 1.60 %, and 2.70 %, respectively, while its recall exceeded the others by 2.27 %–5.52 %. These metrics indicate that Mask R-CNN effectively minimizes false negatives for non-mangrove areas, ensuring robust classification across both mangrove and non-mangrove classes (Table 2).

Examples of segmentation results across various models (Fig. 8A-D) further highlight the spatial advantages of the Mask R-CNN model. Four representative sites with distinct environmental settings were selected for analysis: an estuary with weak tidal dynamics, a bay enclosed by urban development, a delta where mangroves are clearly separated from terrestrial vegetation, and an estuary where mangroves are intermixed with non-mangrove vegetation. When compared to the ground-truth labels, the Mask R-CNN model consistently outperformed other models, particularly in boundary delineation and fine-detail preservation. For instance, Unet exhibited obvious misclassifications in the estuary with weak tidal forces (Fig. 8A), where non-mangrove areas were incorrectly labeled as mangroves. Similarly, in the mixed estuarine environment (Fig. 8D), Unet, FPN, DeepLabV3, and DeepLabV3+ all failed to accurately capture fine-scale mangrove structures and fragmented patches. In contrast, Mask R-CNN effectively mitigated these issues, delivering more precise and detailed segmentation, especially in complex, heterogeneous, or linear mangrove habitats.

Nevertheless, historical mangrove classification using Sentinel imagery still presents inherent challenges due to complex edge structures, fragmented habitat distributions, dynamic intertidal conditions, and varying image quality. These factors demand robust models capable of accurate boundary delineation and class discrimination. Although the 10 m resolution of Sentinel-2 MSI is adequate for regional mangrove mapping, it imposes constraints on detecting small or narrowly distributed patches. Seedling clusters and fine-edge features are susceptible to mixed-pixel effects, which may lead to underestimation of their extent or to boundary misclassification. This spatial limitation can also increase confusion in areas where mangroves exhibit spectral similarity with adjacent vegetation. While the Mask R-CNN mitigates many of these issues by refining object boundaries at the instance level, challenges persist, particularly in delineating sparsely distributed mangrove stands and distinguishing them from spectrally similar plant communities. (Fig. 8). Future improvements could incorporate radar backscatter data from historical Sentinel-1 imagery to extract complementary structural indices and texture features. Moreover, refining feature fusion strategies between shallow and deep network layers may enhance the model's ability to detect subtle and complex mangrove patterns (Zhang et al., 2025). By addressing these aspects, the model could achieve more reliable classification performance and improved adaptability in ecologically heterogeneous and tidally influenced environments.

4.2. *Impacts of suspended sediment concentration*

The growth and maintenance of mangroves are highly dependent on sediment (Phan et al., 2015; Swales et al., 2019), which forms the physical foundation for mangrove colonization, vertical accretion, and

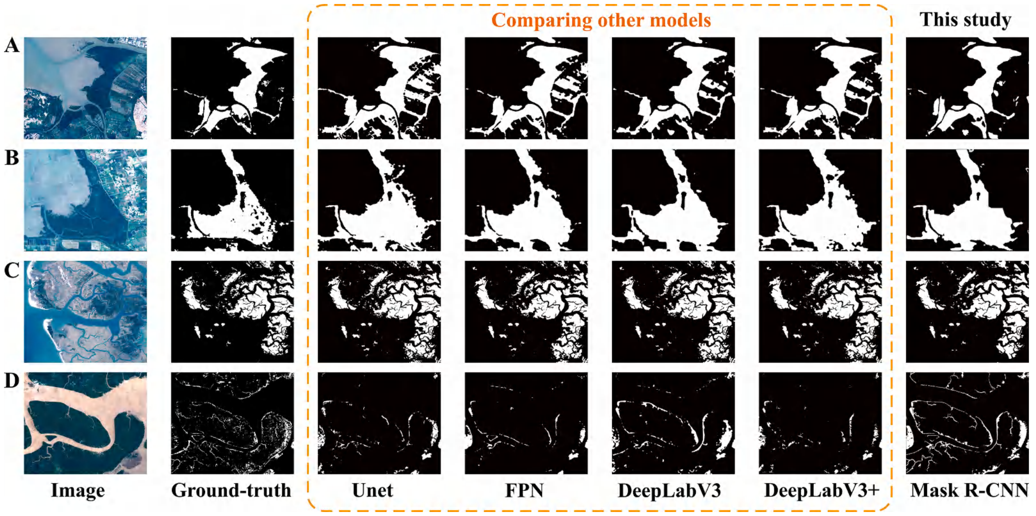

Fig. 8. Comparative segmentation results using different deep learning models. A–D: Representative sites with distinct environmental settings: A) An estuary with weak tidal dynamics; B) A bay enclosed by urban development; C) A delta where mangroves are clearly separated from terrestrial vegetation; D) An estuary where mangroves are intermixed with non-mangrove vegetation.

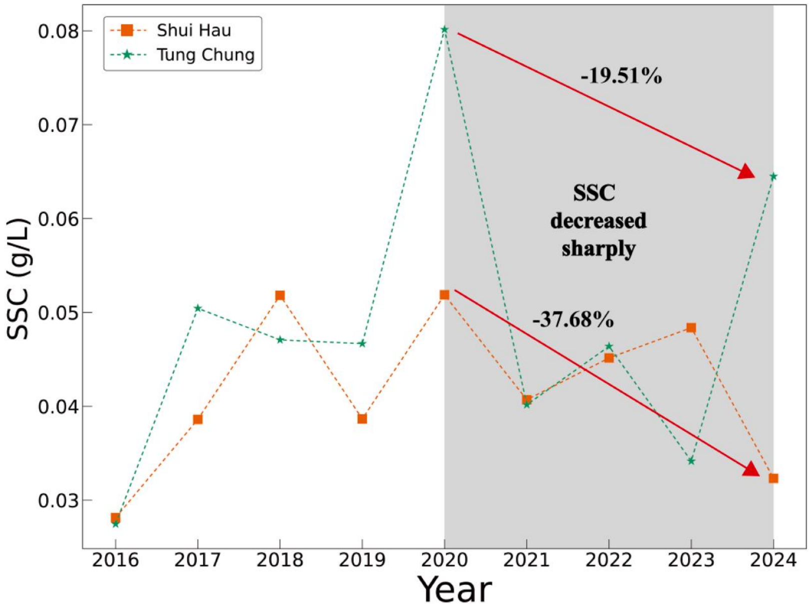

Fig. 9. Temporal trends in suspended sediment concentration in Shui Hau and Tung Chung from 2016 to 2024.

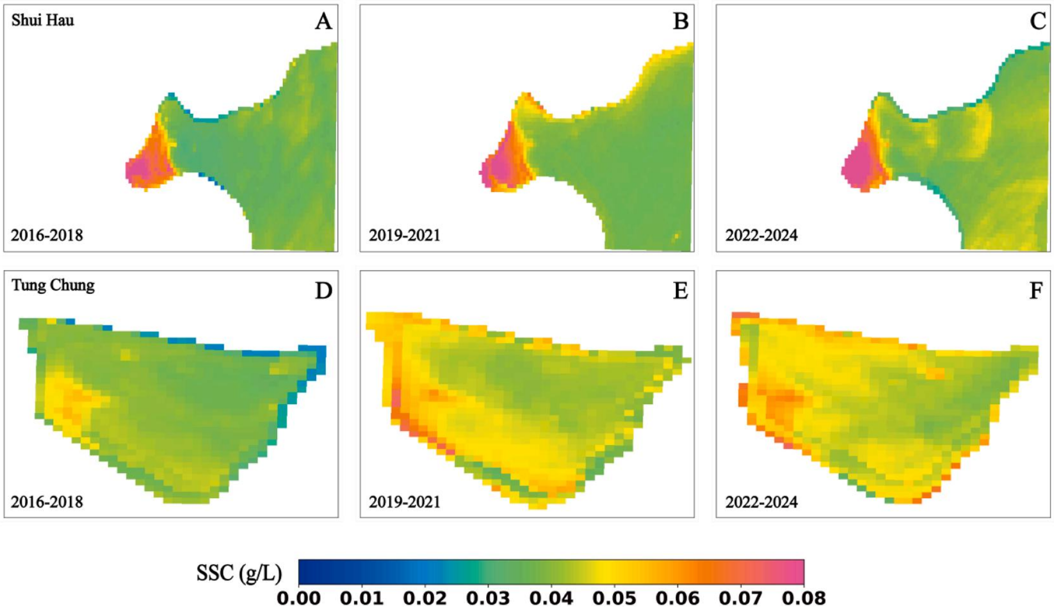

Fig. 10. Estimation of suspended sediment concentration distribution in Shui Hau and Tung Chung from 2016 to 2024.

overall habitat stability. Sediment inputs not only provide essential nutrients and suitable substrates for seedling establishment but also contribute to surface elevation gains that counteract the impacts of sea-level rise (Wu et al., 2025). Adequate and continuous sediment supply enhances root anchorage, promotes sediment trapping by vegetation, and supports the long-term seaward progradation of mangroves (Long et al., 2025). An analysis of suspended sediment concentration (SSC) in Shui Hau and Tung Chung revealed contrasting trends between the two sites. In Shui Hau, SSC increased from 0.028 g/L in 2016 to 0.032 g/L in 2024, while in Tung Chung, SSC rose from 0.027 g/L to 0.065 g/L over the same period (Fig. 9). Notably, regions with higher SSC in both bays largely overlapped with zones of active mangrove growth (Fig. 10). Interestingly, after 2020, SSC levels in both Shui Hau and Tung Chung showed different degrees of decline. In Shui Hau, SSC dropped from 0.052 g/L in 2020 to 0.032 g/L in 2024, representing a 37.68 % decrease. In Tung Chung, SSC decreased from 0.08 g/L to 0.065 g/L, a reduction of 19.51 %. The pronounced rise in SSC before 2020 was likely associated with large-scale reclamation activities related to the construction of the Hong Kong International Airport's (HKIA) third runway. During the reclamation phase, extensive dredging and sediment disturbance introduced substantial quantities of suspended particles into the adjacent coastal waters, temporarily elevating SSC in both Tung Chung and Shui Hau. After the completion of reclamation works around 2020, sediment input to the bays decreased, leading to a gradual recovery of SSC toward pre-construction levels (Fromant et al., 2021; Wang et al., 2023). A reduction in SSC results in diminished sediment deposition on intertidal substrates, which directly weakens the vertical accretion capacity of mangrove habitats. As mangrove root systems rely on continuous sediment burial for anchorage and structural stability, reduced sediment supply leads to weaker root support, making

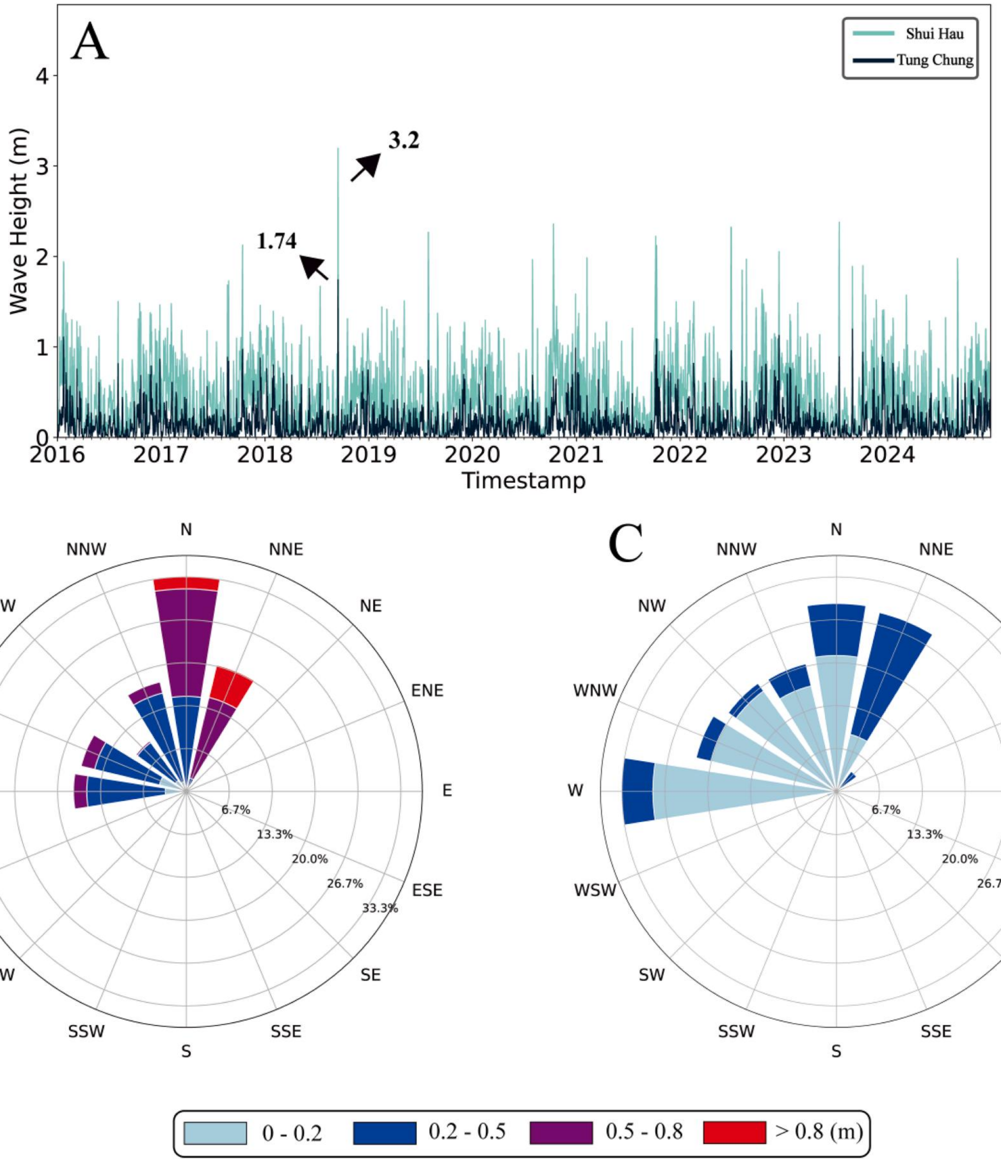

Fig. 11. A: Daily wave heights of the Shui Hau and Tung Chung. B-C: Wave characteristics of the Shui Hau and Tung Chung.

mangroves increasingly susceptible to erosion and physical disturbance (Wang et al., 2025). Meanwhile, Shui Hau experienced significant mangrove loss in the seaward region (subregion 2) between 2018 and 2024 (Fig. 7A), with a continuous decline in TCARI values indicating deteriorating vegetation health. In contrast, although Tung Chung's subregion 2 was disturbed after 2018, TCARI values plateaued rather than continued to rise, suggesting that the decline in SSC may have limited further improvements in vegetation health (Fig. 7B).

Previous studies have shown that sediments can provide space for mangrove colonization and expansion (Wu et al., 2025). For instance, substantial sediment deposition at the Amazon River estuary increased the mangrove area by over 700 km^2 within 12 years (Nascimento et al., 2013). Similarly, sediments delivered by the Ganges and Brahmaputra Rivers promoted vertical accretion, contributing to coastal stabilization in response to postglacial sea-level rise (Wilson and Goodbred, 2015). Therefore, when SSC decreases, the physical environment supporting mangrove development naturally diminishes, leading to corresponding declines in both mangrove health and spatial extent.

4.3. *Impacts of ocean dynamics*

Mangroves growing in intertidal zones with shallow coastal waters are highly susceptible to wave dynamics (Xie et al., 2022). Persistent wave action can erode shorelines, destabilize substrates, and expose mangrove root systems, ultimately leading to mangrove mortality and landward retreat (Wang et al., 2024). Wave direction and SHW analyses for both Shui Hau and Tung Chung sites reveal that waves predominantly approach from the west to east-northeast direction (Fig. 11B–C). However, a striking contrast exists between the two sites in terms of wave energy intensity. As shown in Fig. 11B, Shui Hau faces intense wave energy: only 10.1 % of SHW values are low (0–0.2 m), while 52.5 % fall in the 0.2–0.5 m range and 31.1 % in the 0.5–0.8 m range. Notably, 6.3 % of waves exceed 0.8 m in height. Field observations at Shui Hau reveal exposed air roots of mangroves (Fig. 12A) and stands of mangroves in a dying state (Fig. 12C). In contrast, Tung Chung exhibits much calmer conditions, with 72.7 % of wave heights below 0.2 m, 27.1 % falling between 0.2–0.5 m, and only 0.2 % between 0.5–0.8 m. Importantly, no waves exceeding 0.8 m were recorded at Tung Chung (Fig. 11B–C). Field observations in Tung Chung show the presence of newly established mangrove seedlings expanding seaward (Fig. 12B,

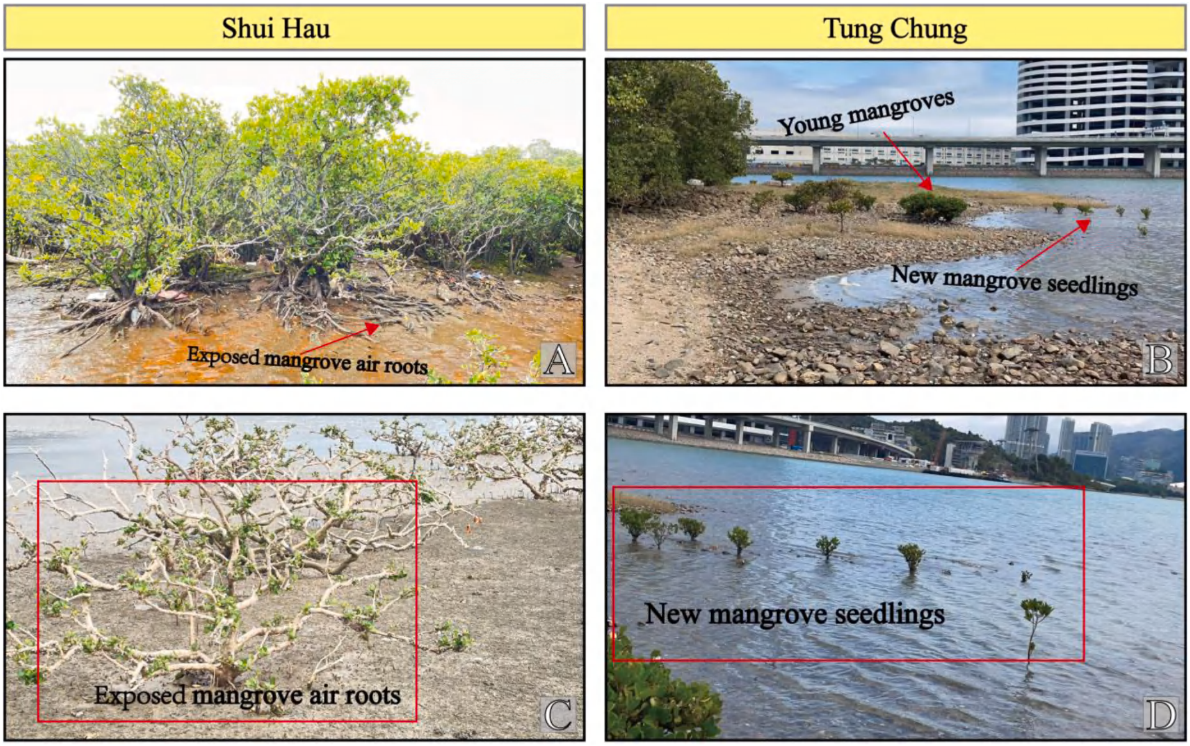

Fig. 12. Photographs of the mangrove sites in Shui Hau and Tung Chung, taken in February 2025.

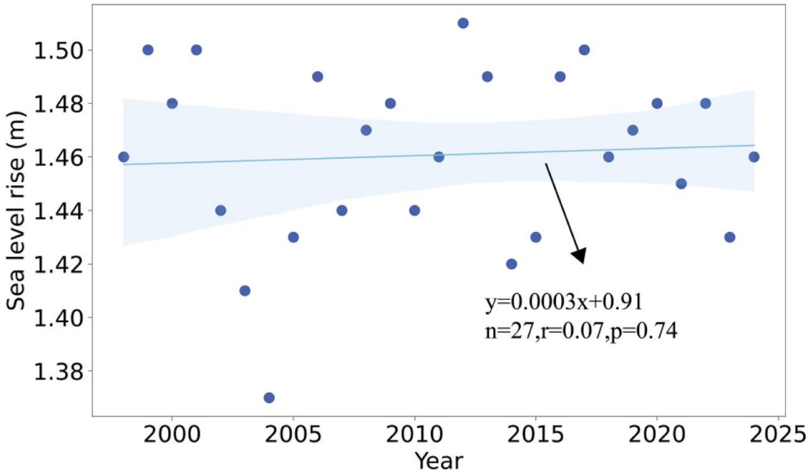

Fig. 13. Sea level rise and its simple linear regression analysis, 1998–2024.

Fig. 12D). The persistent influence of high-energy waves at Shui Hau is likely a major driver of extensive landward mangrove retreat, reflected in the high shoreline erosion rate of −3.37 m/yr, compared to a significantly lower rate of −0.47 m/yr at Tung Chung (Fig. 6A6–B6).As shown in Fig. 11A, both sites experienced a marked spike in SHW in 2018, where Shui Hau reached 3.2 m, and Tung Chung reached 1.74 m, coinciding with the timing of a disturbance observed in Tung Chung's subregion 2. Following this event, TCARI values in that area plateaued, suggesting that wave-induced stress may have halted further improvements in vegetation condition (Fig. 7B).

It is widely acknowledged that rising sea levels driven by global warming pose a significant threat to mangrove ecosystems (Alongi, 2015). Historical records have documented localized and regional extinctions of mangrove forests, primarily triggered by abrupt and rapid sea-level rise events (Cazenave et al., 2014). On Lantau Island, the Shek Pik tide gauge station provides the longest continuous record of sea level, offering valuable insights into long-term coastal dynamics. According to measurements of mean sea level trends from this station, sea levels at both Shui Hau and Tung Chung have exhibited a relatively stable pattern over the past nearly three decades (Fig. 13). The calculated rate of mean sea-level rise is 0.3 mm/yr, indicating a slow and stable change over time. Additionally, the average vertical sediment accumulation rates, derived from the mean slope of the DEM data, were 12.36 mm/yr at Tung Chung and 3.84 mm/yr at Shui Hau, both of which far exceed the rate of sea-level rise. This suggests that mangroves in these two regions are currently not under threat from sea-level rise. Although the long-term sea-level record indicates a stable and slow rate of rise for the past 27 years (Fig. 13), it should be acknowledged that future accelerations in regional sea-level rise cannot be fully ruled out. Moreover, tide-gauge data represent relative sea level at a fixed point

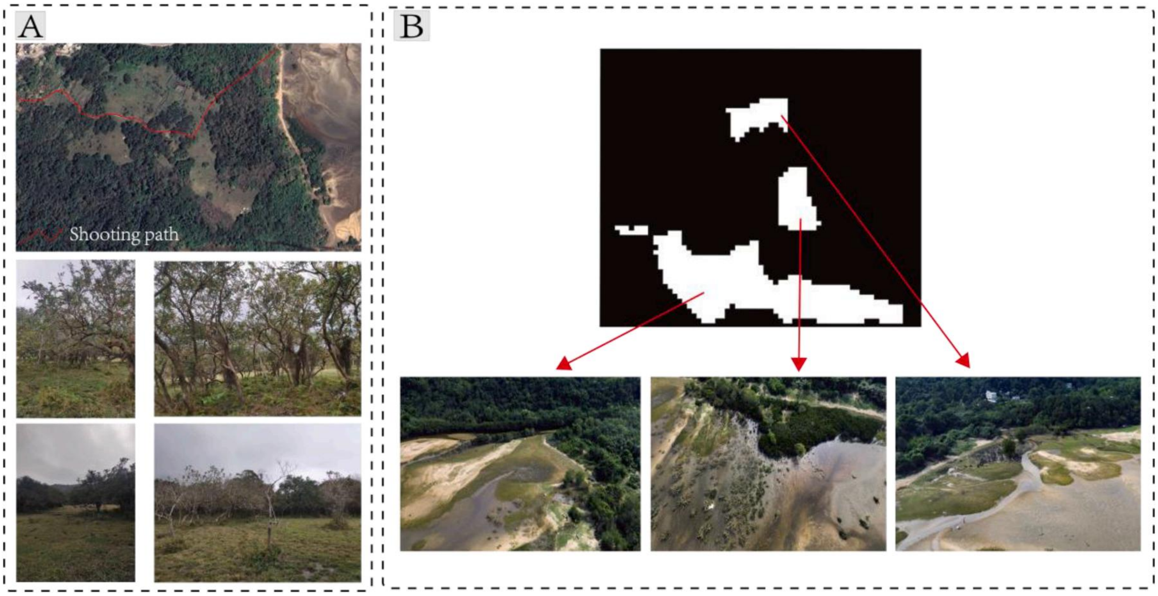

Fig. 14. A: Field survey route and ground photographs along the shooting path in the Shui Hau. B: Comparison between MIM-delineated mangrove patches and corresponding Google map images acquired in 2020 (from Google map).

and may not capture short-term extremes or localized subsidence effects. Therefore, while current trends suggest limited risk, continued monitoring remains essential.

4.4. Dataset discrepancies and segmentation challenges of the MIM

The visual comparison reveals evident discrepancies between the MIM-derived results and the LREIS Global Mangrove dataset (2018–2020) as well as the LUHK dataset in the Shui Hau area, particularly regarding fragmented and dying mangrove patches (Fig. 4). Such inconsistencies are not uncommon among high-resolution mangrove datasets (Zhang et al., 2025), largely due to mixed pixel effects and insufficient spatial resolution. To verify the accuracy of our MIM results, we conducted field observations along the mangrove zones delineated by the LREIS dataset. The field survey confirmed that most of the areas classified as mangrove by LREIS in Shui Hau were in fact non-mangrove vegetation rather than true mangroves (Fig. 14A). Moreover, the LUHK dataset aggregated mangrove and swamp vegetation into a single class and left portions of the Shui Hau coastal zone unmapped. In contrast, MIM accurately delineated fragmented mangrove patches that corresponded well with ground photographs from Google map acquired in 2020 (Fig. 14B), effectively capturing the spatial heterogeneity of these small patches. By leveraging multi-spectral Sentinel-2 imagery, elevation data, and the instance segmentation capability of Mask R-CNN, MIM achieves pixel-level boundary precision and enhanced discrimination of sparse mangrove assemblages. This improvement is particularly evident in ecologically complex zones, where conventional semantic segmentation or low-resolution global datasets struggle to identify narrow and fragmented patches. This capability is crucial for establishing a continuous, temporally consistent mangrove monitoring framework that can support long-term assessments of degradation and recovery dynamics across Hong Kong's coastal wetlands.

Despite these strengths, several segmentation challenges were observed in vegetation-complex environments. As shown in Fig. 8, misclassifications occasionally occurred in transitional zones where mangroves co-exist with saltmarsh plants or low shrubs that exhibit similar spectral characteristics. Shadows, tidal water influence, and mixed-pixel effects further reduced separability along fine boundaries, resulting in slight over- or under-segmentation in some cases. Small and sparsely distributed seedling clusters were also difficult to detect consistently due to their limited canopy size relative to the 10 m Sentinel-2 resolution (Fig. 4). In addition, the use of the 30 m Copernicus DEM introduces an inherent scale mismatch with the 10 m Sentinel-2 imagery. Although elevation varies gradually across coastal landscapes and can still provide meaningful low-frequency topographic context (Fereshtehpour et al., 2024), the coarser DEM resolution may limit the model's ability to capture fine-scale elevation differences along narrow tidal flats or embankments. This limitation suggests that future work could benefit from incorporating higher-resolution DEM or LiDAR-derived elevation data to further improve boundary delineation in complex micro-topographic environments.

Beyond methodological considerations, the spatial patterns identified by the MIM also hold direct relevance for mangrove management. Areas exhibiting persistent shoreline retreat or negative vegetation trends can serve as priority zones for targeted restoration or sediment supplementation. Conversely, regions showing natural recovery may provide suitable reference sites for informing restoration design and evaluating conservation effectiveness. These insights can assist managers in allocating resources and developing adaptive strategies to safeguard mangrove resilience under ongoing environmental change.

5. Conclusions

By integrating deep learning, shoreline change modeling, SSC estimation, and vegetation health assessment, this study offers a comprehensive framework for long-term mangrove monitoring under data-scarce and morphologically complex conditions. The main findings can be shown as follows:

1. We established a high-precision mangrove identification model by applying the Mask R-CNN framework with Sentinel-2 imagery, achieving a **MAPE of 6.91 %** and outperforming semantic segmentation models (e.g., Unet, DeepLabV3+) in delineating fragmented mangrove patches with complex boundaries.
2. The two representative mangrove stands on Lantau Island exhibited markedly divergent trends during 2016–2024. At Shui Hau, mangrove area experienced continuous decline from 0.77 ha to 0.39 ha, representing a substantial reduction of 49 %, accompanied by shoreline retreat at an average rate of 3.07 m/yr, indicating severe erosional degradation. In striking contrast, Tung Chung

demonstrated steady mangrove expansion from 3.28 ha to 3.59 ha (9.5 % increase), with shoreline progradation occurring at 0.85 m/yr, reflecting favorable developmental conditions.

3. The spatial divergence in mangrove dynamics between these two sites was primarily governed by distinct hydrodynamic and sedimentary regimes. At Shui Hau, high wave exposure coupled with declining suspended sediment concentration (SSC) contributed to habitat fragmentation and exacerbated shoreline erosion. In contrast, Tung Chung benefited from more moderate wave regimes and favorable sediment dynamics, which provided stable sedimentary substrates facilitating natural mangrove expansion. This striking contrast underscores the critical control of wave-sediment coupling processes on mangrove succession patterns.

The results underscore the importance of high-resolution historical mapping in supporting adaptive conservation strategies. For future management, targeted restoration efforts should prioritize erosion-prone areas such as Shui Hau, while maintaining natural expansion in regions like Tung Chung. Community engagement and the protection of sediment delivery pathways will be key to enhancing mangrove resilience against anthropogenic and climatic pressures.

Declaration of generative AI and AI-assisted technologies in the writing process

During the preparation of this work the authors used ChatGPT (OpenAI) in order to improve the language and readability of the manuscript. After using this tool, the authors reviewed and edited the content as needed and take full responsibility for the content of the publication.

CRediT authorship contribution statement

Renjie Wu: Writing – review & editing, Writing – original draft, Visualization, Validation, Software, Resources, Methodology, Data curation. **Zhijun Dai:** Writing – original draft, Visualization, Validation, Conceptualization. **Xuefei Mei:** Visualization, Validation, Software. **Chuqi Long:** Visualization, Validation, Software. **Diankai Wang:** Validation, Software, Methodology. **Jie Wang:** Visualization, Validation, Methodology. **Jinping Cheng:** Visualization, Validation.

Declaration of competing interest

To whom it may concerns: The authors declare that there are no conflicts of interest regarding the submitted paper “Mask R-CNN-Based Detection and Segmentation of Mangrove Ecosystems in Lantau Island, Hong Kong”.

Acknowledgments

This research was supported by the National Natural Science Key Foundation of China (NSFC) (41930537) and Shanghai International Science and Technology Cooperation Fund Project (23230713800). The Croucher Foundation Visitorship for PRC Scholars (2025/26) provided funding support to Dr. Jinping Cheng at the Education University of Hong Kong to host Prof. Xuefei Mei from the East China Normal University.

Data availability

Data will be made available on request.

References

Alongi, D.M., 2015. The impact of climate change on mangrove forests. Curr. Clim. Chang. Rep. 1, 30–39.

Anees, S.A., Mehmood, K., Khan, W.R., Shahzad, F., Zhran, M., Ayub, R., Alarfaj, A.A., Alharbi, S.A., Liu, Q., 2025. Spatiotemporal dynamics of vegetation cover: integrative machine learning analysis of multispectral imagery and environmental predictors. Earth Sci. Inform. 18, 152–175.

Baloloy, A.B., Blanco, A.C., Ana, R.R.C.S., Nadaoka, K., 2020. Development and application of a new mangrove vegetation index (MVI) for rapid and accurate mangrove mapping. ISPRS J. Photogramm. Remote Sens. 166, 95–117.

Blankespoor, B., Dasgupta, S., Lange, G.-M., 2017. Mangroves as a protection from storm surges in a changing climate. Ambio 46, 478–491.

Bunting, P., Rosenqvist, A., Hilarides, L., Lucas, R.M., Thomas, N., Tadono, T., Worthington, T.A., Spalding, M., Murray, N.J., Rebelo, L.-M., 2022. Global mangrove extent change 1996–2020: global mangrove watch version 3.0. Remote Sens. 14, 3657.

Carruthers, L., Ersek, V., Maher, D., Sanders, C., Tait, D., Soares, J., Floyd, M., Hashim, A. S., Helber, S., Garnett, M., East, H., Johnson, J.A., Ponta, G., Sippo, J.Z., 2024. Sea-level rise and extreme indian ocean dipole explain mangrove dieback in the Maldives. Sci. Rep. 14 (1), 27012.

Carvalho, O.L.F.D., De Carvalho Júnior, O.A., Albuquerque, A.O.D., Bem, P.P.D., Silva, C. R., Ferreira, P.H.G., Moura, R.D.S.D., Gomes, R.A.T., Guimarães, R.F., Borges, D.L., 2020. Instance segmentation for large, multi-channel remote sensing imagery using mask-RCNN and a mosaicking approach. Remote Sens. 13 (1), 39.

Cazenave, A., Dieng, H.-B., Meyssignac, B., Von Schuckmann, K., Decharme, B., Berthier, E., 2014. The rate of sea-level rise. Nat. Clim. Chang. 4, 358–361.

Chandrasekar, K., Sesha Sai, M.V.R., Roy, P.S., Dwevedi, R.S., 2010. Land surface water index (LSWI) response to rainfall and NDVI using the MODIS vegetation index product. Int. J. Remote Sens. 31, 3987–4005.

Chen, B., Dong, J., Thi Thu Hien, T., Yun, T., Kou, W., Wu, Z., Yang, C., Wang, G., Lai, H., Liu, R., An, F., 2025. A full time series imagery and full cycle monitoring (FTSI-FCM) algorithm for tracking rubber plantation dynamics in the Vietnam from 1986 to 2022. ISPRS J. Photogramm. Remote Sens. 220, 377–394.

Donato, D.C., Kauffman, J.B., Murdiyarso, D., Kurnianto, S., Stidham, M., Kanninen, M., 2011. Mangroves among the most carbon-rich forests in the tropics. Nat. Geosci. 4 (5), 293–297.

Duarte, C.M., Losada, I.J., Hendriks, I.E., Mazarrasa, I., Marbà, N., 2013. The role of coastal plant communities for climate change mitigation and adaptation. Nat. Clim. Chang. 3 (11), 961–968.

Dzulfigar, A., Asy'Ari, R., Rahmawati, A.D., Ulfa, A., Marfi, K.P., Puspitasari, R.F., Setiawan, Y., 2024. Spatio-temporal analysis of mangroves in Subang Regency using Sentinel-2 TimeSeries Data. SSRS J. A 2, 28–47.

Ellison, A.M., Felson, A.J., Friess, D.A., 2020. Mangrove rehabilitation and restoration as experimental adaptive management. Front. Mar. Sci. 7.

Fanous, M., Eden, J.M., Remesan, R., Daneshkhah, A., 2023. Challenges and prospects of climate change impact assessment on mangrove environments through mathematical models. Environ. Model. Softw. 162, 105658.

Fereshtehpour, M., Esmaeilzadeh, M., Alipour, R.S., Burian, S.J., 2024. Impacts of DEM type and resolution on deep learning-based flood inundation mapping. Earth Sci. Inform. 17, 1125–1145.

Friess, D.A., Rogers, K., Lovelock, C.E., Krauss, K.W., Hamilton, S.E., Lee, S.Y., Lucas, R., Primavera, J., Rajkaran, A., Shi, S., 2019. The state of the world’s mangrove forests: past, present, and future. Annu. Rev. Environ. Resour. 44 (1), 89–115.

Fromant, G., Le Dantec, N., Perrot, Y., Floc'h, F., Lebourges-Dhaussy, A., Delacourt, C., 2021. Suspended sediment concentration field quantified from a calibrated MultiBeam EchoSounder. Appl. Acoust. 180, 108107.

Gilman, E., Ellison, J., Coleman, R., 2007. Assessment of mangrove response to projected relative sea-level rise and recent historical reconstruction of shoreline position. Environ. Monit. Assess. 124 (1–3), 105–130.

Giri, C., 2016. Observation and monitoring of mangrove forests using remote sensing: opportunities and challenges. Remote Sens. 8 (9), 783–791.

Giri, C., Ochieng, E., Tieszen, L.L., Zhu, Z., Singh, A., Loveland, T., Masek, J., Duke, N., 2011. Status and distribution of mangrove forests of the world using earth observation satellite data. Glob. Ecol. Biogeogr. 20 (1), 154–159.

Goldberg, L., Lagomasino, D., Thomas, N., Fatoyinbo, T., 2020. Global declines in human-driven mangrove loss. Glob. Chang. Biol. 26 (10), 5844–5855.

Hagger, V., Worthington, T.A., Lovelock, C.E., Adame, M.F., Amano, T., Brown, B.M., Friess, D.A., Landis, E., Mumby, P.J., Morrison, T.H., O’Brien, K.R., Wilson, K.A., Zganjar, C., Saunders, M.I., 2022. Drivers of global mangrove loss and gain in social-ecological systems. Nat. Commun. 13 (1).

Hamer, E., Oyedotun, T.D.T., Charles, E., Moonsammy, S., 2024. Spatio-temporal analysis of mangrove ecosystems and hydrological regimes in coastal Guyana using remote sensing. J. Coast. Res. (113), 544–548. Special Issue No.

Han, Q., Yin, Q., Zheng, X., Chen, Z., 2022. Remote sensing image building detection method based on mask R-CNN. Complex Intell. Syst. 8 (3), 1847–1855.

He, K., Gkioxari, G., Dollár, P., Girshick, R., 2017. Mask r-cnn. In: Proceedings of the IEEE international conference on computer vision, pp. 2961–2969.

Himmelstoss, E.A., Henderson, R.E., Kratzmann, M.G., Farris, A.S., 2021. Digital Shoreline Analysis System (DSAS) Version 5.1 User Guide. US Geological Survey, p. 1091, 2021-.

Ho, J.T.W., Chung, T.W.L., 2025. Dynamics and discrepancies in rural–urban village regeneration: a case study of a coastal community in Hong Kong SAR, China. J. Chin. Archit. Urban. 7, 4992.

Huete, A., Didan, K., Miura, T., Rodriguez, E.P., Gao, X., Ferreira, L.G., 2002. Overview of the radiometric and biophysical performance of the MODIS vegetation indices. Remote Sens. Environ. 83 (1–2), 195–213.

Jennerjahn, T.C., Ittekkot, V., 2002. Relevance of mangroves for the production and deposition of organic matter along tropical continental margins. Naturwissenschaften 89 (1), 23–30.

Jia, M., Wang, Z., Li, L., Song, K., Ren, C., Liu, B., Mao, D., 2014. Mapping China's mangroves based on an object-oriented classification of landsat imagery. Wetlands 34 (2), 277–283.

Kauffman, J.B., Cole, T.G., 2010. Micronesian mangrove forest structure and tree responses to a severe typhoon. Wetlands 30 (6), 1077–1084.

Kennedy, R.E., Yang, Z., Cohen, W.B., 2010. Detecting trends in forest disturbance and recovery using yearly landsat time series: 1. LandTrendr — temporal segmentation algorithms. Remote Sens. Environ. 114 (12), 2897–2910.

Kirui, K.B., Kairo, J.G., Bosire, J., Viergever, K.M., Rudra, S., Huxham, M., Briers, R.A., 2013. Mapping of mangrove forest land cover change along the Kenya coastline using landsat imagery. Ocean Coast. Manag. 83, 19–24.

Krauss, K.W., McKee, K.L., Lovelock, C.E., Cahoon, D.R., Saintilan, N., Reef, R., Chen, L., 2014. How mangrove forests adjust to rising sea level. New Phytol. 202 (1), 19–34.

Lassalle, G., De Souza Filho, C.R., 2022. Tracking canopy gaps in mangroves remotely using deep learning. Remote Sens. Ecol. Conserv. 8 (6), 890–903.

Leal, M., Spalding, M.D., 2022. The State of the World's Mangroves 2022. Global Mangrove Alliance.

Liang, X., Dai, Z., Mei, X., Wang, R., Zeng, W., Fagherazzi, S., 2025. Hurricanes induced irreversible large-scale loss of mangrove forests. Geophys. Res. Lett. 52 (9).

Liu, Y., Yao, X., Gu, Z., Zhou, Z., Liu, X., Chen, X., Wei, S., 2022. Study of the automatic recognition of landslides by using InSAR images and the improved mask R-CNN model in the eastern tibet plateau. Remote Sens. 14 (14), 3362.

Long, C., Dai, Z., Mei, X., Liang, X., Zhang, X., Xi, Y., Wang, R., Binh, N.A., Van, C.M., Cheng, J., 2025. Machine learning-based detection of dynamic changes in mangrove forest, Beilun estuary. Ocean Coast. Manag. 266, 107696.

Luo, W., Shen, F., He, Q., Cao, F., Zhao, H., Li, M., 2022. Changes in suspended sediments in the Yangtze River estuary from 1984 to 2020: responses to basin and estuarine engineering constructions. Sci. Total Environ. 805, 150381.

Mbense, S., Rajkaran, A., Bolosha, U., Adams, J., 2016. Rapid colonization of degraded mangrove habitat by succulent salt marsh. S. Afr. J. Bot. 107, 129–136.

Mehmood, K., Anees, S.A., Muhammad, S., Shahzad, F., Liu, Q., Khan, W.R., Shrahili, M., Ansari, M.J., Dube, T., 2025. Machine learning and spatio temporal analysis for assessing ecological impacts of the billion tree afforestation project. Ecol. Evol. 15, e70736.

Monika, Yadav, A., 2022. A holistic study on impact of anthropogenic activities over the mangrove ecosystem and their conservation strategies. Coastal Ecosystems: Environmental Importance, Current Challenges and Conservation Measures, pp. 265–284.

Nascimento, W.R., Souza-Filho, P.W.M., Proisy, C., Lucas, R.M., Rosenqvist, A., 2013. Mapping changes in the largest continuous amazonian mangrove belt using object-based classification of multisensor satellite imagery. Estuar. Coast. Shelf Sci. 117, 83–93.

Ofori, S.A., Asante, F., Boateng, T.A.B., Adu-Asare, A., Dahdouh-Guebas, F., 2025. Spatiotemporal changes in Ghana's mangrove ecosystems and pathways for restoration action. Aquat. Conserv. 35 (7), e70187.

Paling, E.I., Kobryn, H.T., Humphreys, G., 2008. Assessing the extent of mangrove change caused by cyclone vance in the eastern exmouth gulf, northwestern Australia. Estuar. Coast. Shelf Sci. 77 (4), 603–613.

Pan, Y., Shen, F., Wei, X., 2018. Fusion of landsat-8/OLI and GOCI data for hourly mapping of suspended particulate matter at high spatial resolution: a case study in the Yangtze (changjiang) estuary. Remote Sens. (Basel) 10 (2), 158.

Phan, L.K., van Thiel de Vries, J.S., Stive, M.J., 2015. Coastal mangrove squeeze in the Mekong Delta. J. Coast. Res. 31 (2), 233–243.

Phiri, D., Simwanda, M., Salekin, S., Nyirenda, V., Murayama, Y., Ranagalage, M., 2020. Sentinel-2 data for land cover/use mapping: a review. Remote Sens. (Basel) 12 (14), 2291.

Raw, J.L., Godbold, J.A., Van Niekerk, L., Adams, J.B., 2019. Drivers of mangrove distribution at the high-energy, wave-dominated, southern African range limit. Estuar. Coast. Shelf Sci. 226, 106296.

Richards, D.R., Thompson, B.S., Wijedasa, L., 2020. Quantifying net loss of global mangrove carbon stocks from 20 years of land cover change. Nat. Commun. 11 (1).

Robertson, A.I., Daniel, P.A., Dixon, P., 1991. Mangrove forest structure and productivity in the fly river estuary, papua new guinea. Mar. Biol. 111 (1), 147–155.

Sharifi, A., 2020. Remotely sensed vegetation indices for crop nutrition mapping. J. Sci. Food Agric. 100 (14), 5191–5196.

Swales, A., Reeve, G., Cahoon, D.R., Lovelock, C.E., 2019. Landscape evolution of a fluvial sediment-rich avicennia marina mangrove forest: insights from seasonal and inter-annual surface-elevation dynamics. Ecosystems 22 (6), 1232–1255.

Tam, N.F.Y., Wong, Y.-S., Lu, C.Y., Berry, R., 1997. Mapping and characterization of mangrove plant communities in Hong Kong. In: Wong, Y.-S., Tam, N.F.-Y. (Eds.), Asia-Pacific Conference on Science and Management of Coastal Environment. Netherlands, Dordrecht. Springer, pp. 25–37.

Tang, R., Shen, F., Pan, Y., Ruddick, K., Shang, P., 2019. Multi-source high-resolution satellite products in Yangtze estuary: cross-comparisons and impacts of signal-to-noise ratio and spatial resolution. Opt. Express 27 (5), 6426.

Vorsatz, L.D., So, M.W.K., Not, C., Cannicci, S., 2023. Anthropogenic debris pollution in peri-urban mangroves of south China: spatial, seasonal, and environmental drivers in Hong Kong. Mar. Pollut. Bull. 195, 115495.

Walsh, J.P., Ridd, P.V., 2008. Processes, sediments, and stratigraphy of the Fly River Delta. Dev. Earth Environ. Sci. 9, 153–176.

Wang, D., Dai, Z., Long, C., Liang, X., Xiong, Y., Cheng, J., 2025. The serious loss of mangrove forest over the largest delta of Africa, Niger delta: causes and reasons. Mar. Environ. Res. 210, 107350.

Wang, D., He, D., 2022. Fusion of mask RCNN and attention mechanism for instance segmentation of apples under complex background. Comput. Electron. Agric. 196, 106864.

Wang, H., Xie, M., Chen, O., Zhou, Z., Cao, H., Wei, W., 2024. Investigation on the soil resistance to wave-induced lateral erosion under different mangrove forests. J. Sea Res. 200, 102517.

Wang, Z., Mao, Z., Zhang, L., Zhang, X., Yuan, D., Li, Y., Wu, Z., Huang, H., Zhu, Q., 2023. Observations of the impacts of hong kong international airport on water quality from 1986 to 2022 using landsat satellite. Remote Sens. 15 (12), 3146.

Ward, R.D., Friess, D.A., Day, R.H., Mackenzie, R.A., 2016. Impacts of climate change on mangrove ecosystems: a region by region overview. Ecosyst. Health Sustain. 2 (4).

Wilson, C.A., Goodbred, S.L., 2015. Construction and maintenance of the ganges-brahmaputra-meghna delta: linking process, morphology, and stratigraphy. Annu. Rev. Mar. Sci. 7 (1), 67–88.

Wolanski, E., Williams, D., Hanert, E., 2006. The sediment trapping efficiency of the macro-tidal daly estuary, tropical australia. Estuar. Coast. Shelf Sci. 69 (1–2), 291–298.

Woodroffe, C.D., Rogers, K., McKee, K.L., Lovelock, C.E., Mendelssohn, I.A., Saintilan, N., 2016. Mangrove sedimentation and response to relative sea-level rise. Annu. Rev. Mar. Sci. 8 (1), 243–266.

Wu, Q., 2020. geemap: a python package for interactive mapping with Google earth engine. J. Open Source Softw. 5 (51), 2305.

Wu, Q., 2025. GeoAI: a Python package for integrating artificial intelligence with geospatial data analysis and visualization. J. Open Source Softw. 9025.

Wu, R., Dai, Z., Mei, X., Luo, J., Fagherazzi, S., 2025. Profiling of mangrove forest dynamics in the fly river delta, Papua new guinea. Mar. Pollut. Bull. 217, 118119.

Xiao, H., Su, F., Fu, D., Yu, H., Ju, C., Pan, T., Kang, L., 2021. 10-m global mangrove classification products of 2018-2020 based on big data. Sci. Data Bank.

Xie, D., Schwarz, C., Kleinhans, M.G., Zhou, Z., Van Maanen, B., 2022. Implications of coastal conditions and sea-level rise on mangrove vulnerability: a bio-morphodynamic modeling study. J. Geophys. Res. Earth Surf. 127 (3), e2021JF006301.

Xiong, Y., Dai, Z., Long, C., 2024. Machine Learning-Based examination of recent mangrove forest changes in the western Irrawaddy River Delta, Southeast Asia. Catena 234, 107601.

Xiong, H., Zong, Y., Huang, G., Fu, S., 2018. Sedimentary responses to Holocene sea-level change in a shallow marine environment of southern China. J. Asian Earth Sci. 166, 95–106.

Xu, C., Wang, J., Sang, Y., Li, K., Liu, J., Yang, G., 2023. An effective deep learning model for monitoring mangroves: A case study of the Indus Delta. Remote Sens 15, 2220.

Yin, C., Tang, J., Yuan, T., Xu, Z., Wang, Y., 2022. Bridging the gap between semantic segmentation and instance segmentation. IEEE Trans. Multimed. 24, 4183–4196.

Zhang, H.W., Wei, S., Liang, X., Chen, Y., Zhang, H.S., 2025. Scale effects in mangrove mapping from ultra-high-resolution remote sensing imagery. Int. J. Appl. Earth Obs. Geoinform. 136, 104310.

Zhang, Y.-F., Ren, W., Zhang, Z., Jia, Z., Wang, L., Tan, T., 2022. Focal and efficient IOU loss for accurate bounding box regression. Neurocomputing 506, 146–157.

Zhang, Z., Ahmed, M.R., Zhang, Q., Li, Y., Li, Y., 2023. Monitoring of 35-year mangrove wetland change dynamics and agents in the sundarbans using temporal consistency checking. Remote Sens. 15 (3), 625.

Zhao, T., Wang, S., Ouyang, C., Chen, M., Liu, C., Zhang, J., Wang, L., 2024. Artificial intelligence for geoscience: Progress, challenges, and perspectives. Innovation 5 (5), 100691.

Zheng, Z., Ren, J., Li, Y., Huang, C., Liu, G., Du, C., Lyu, H., 2016. Remote sensing of diffuse attenuation coefficient patterns from landsat 8 OLI imagery of turbid inland waters: a case study of dongting lake. Sci. Total Environ. 573, 39–54.